Lamellipodium tip actin barbed ends serve as a force sensor

Kazuma Koseki[1], Daisuke Taniguchi[1], Sawako Yamashiro[1,2], Hiroaki Mizuno[2], Dimitrios Vavylonis[3], Naoki Watanabe[1,2,4]

[1] Department of Pharmacology, Kyoto University Graduate School of Medicine

[2] Laboratory of Single-Molecule Cell Biology, Kyoto University Graduate School of Biostudies

[3] Department of Physics, Lehigh University

[4] To whom correspondence should be addressed.

E-mail: watanabe.naoki.4v@kyoto-u.ac.jp

Yoshida-Konoe-cho, Sakyo-ku, Kyoto, 606-8501, Japan

Tel 81-75-753-4396, Fax 81-75-753-4394

Abstract

Cells change direction of migration by sensing rigidity of environment and traction force, yet its underlying mechanism is unclear. Here we show that tip actin barbed ends serve as an active 'force sensor' at the leading edge. We established a method to visualize intracellular single-molecule fluorescent actin through an elastic culture substrate. We found that immediately after cell edge stretch, actin assembly increased specifically at the lamellipodium tip. The rate of actin assembly increased with increasing stretch speed. Furthermore, tip actin polymerization remained elevated at the subsequent hold step, which was accompanied by a decrease in the load on the tip barbed ends. Stretch-induced tip actin polymerization was still observed without either the WAVE complex or Ena/VASP proteins. The observed relationships between forces and tip actin polymerization are consistent with a force-velocity relationship as predicted by the Brownian ratchet mechanism. Stretch caused extra membrane protrusion with respect to the stretched substrate and increased local tip polymerization by >5% of total cellular actin in 30 sec. Our data reveal that augmentation of lamellipodium tip actin assembly is directly coupled to the load decrease, which may serve as a force sensor for directed cell protrusion.

KEYWORDS

Actin polymerization, lamellipodium tip, mechanosense, Brownian ratchet, single-molecule speckle microscopy

1 | INTRODUCTION

Cells collect information about outer environment for their functions. Information, in a narrow sense, is the input into the sensory systems composed of 'receptor' molecules. In addition to chemical signals, cells sense mechanical properties of outer environment to change morphology, direction of migration, proliferation and differentiation (Engler *et al.* 2006). One example is found in durotaxis (Lo *et al.* 2000). In durotaxis, migration of fibroblasts is guided to stiff culture substrates. Immediately after the lamellipodium edge makes contact with the stiff substrate, the cell edge protrudes before translocation of the cell body (Lo *et al.* 2000) (http://users.ece.cmu.edu/~yuliwang/Videos/Migration/Durotaxis.html), suggesting that the sensing mechanism(s) exists at the cell periphery. Another is found in the tension-driven axonal growth. Application of traction force to the tip of a neurite in cultured neurons induces neurite extension and differentiation into an axon (Bray 1984), which continues 1-3 days after removal of the micromanipulation needle (Lamoureux *et al.* 2002).

The force generation at the cell leading edge is theorized by Brownian ratchet (BR) models (Peskin *et al.* 1993; Mogilner & Oster 1996, 2003). These models predict force generation by stochastic intercalation of actin monomers between the plasma membrane

and the actin filament tip. Free energy is provided by actin polymerization, which is facilitated by abundant profilin-actin complex *in vivo*. Several studies have reported the force-velocity relationship in *in vitro* actin-based motility of *Listeria monocytogenes* (McGrath *et al.* 2003) and particles coated with N-WASP (Wiesner *et al.* 2003). In particular, an increase in F-actin mass upon lowering of the force is observed on the surface of magnetic particles (Demoulin *et al.* 2014), although it remains elusive whether augmentation is solely due to decreased loads on the filament end. To elucidate the traction force regulation of cell protrusion *in vivo*, direct monitoring of force-coupled actin polymerization and its comparison with the velocity of the retrograde actin flow are crucial.

To precisely quantify actin polymerization during cell edge stretch, we developed a method enabling fluorescent single-molecule speckle (SiMS) microscopy (Watanabe & Mitchison 2002; Yamashiro *et al.* 2014) through a thin layer (≈50 μm thick) of polydimethylsiloxane (PDMS) silicone rubber. Our method avoids direct contact of the manipulation needle on the cell surface which was employed in the previous studies (Riveline *et al.* 2001; Heinemann *et al.* 2011; Houk *et al.* 2012; Mueller *et al.* 2017) because we noticed that direct needle contact rapidly reduces F-actin density in lamellipodia (Figure S1 and S2). Moreover, direct mechanical strain on the cell surface

triggers processive actin nucleation by formin homology proteins (Higashida *et al.* 2013; Watanabe *et al.* 2018). It is also important to monitor fluorescently-tagged actin directly because distribution of F-actin binding probes including Lifeact could be affected by the retrograde actin flow speed due to convection-induced mislocalization in live cells (Yamashiro *et al.* 2019; Yamashiro & Watanabe 2019). Instead in this study, we applied traction force to the cell edge by pulling the culture substrate nearby. We used PDMS coated with poly-L-lysine (PLL). Single-molecule imaging through thick specimens has been difficult due to spherical aberration of high numerical aperture objectives. Recently-developed silicone oil objectives optimized for the refractive index of cell and tissue samples (≈1.4), which is close to that of PDMS (1.41) (Cai *et al.* 2013), greatly improved signal detection. Our improved microscopy (eSiMS) (Yamashiro *et al.* 2014) using bright, photostable DyLight550-labeled actin (DL-actin) allowed robust detection of single-molecules of actin. Combining these techniques, we succeeded in visualizing single-molecule speckles of fluorescent actin (actin SiMS) at the stretched cell periphery. This enabled us to examine the effect of a decrease in the load on the leading edge actin barbed end (down to zero), which contrasts with the previous studies focusing on near stall forces of actin elongation (Parekh *et al.* 2005; Prass *et al.* 2006; Footer *et al.* 2007; Heinemann *et al.* 2011; Zimmermann *et al.* 2012; Bieling *et al.* 2016).

The present study reveals a relationship between external force and tip actin polymerization at the stretched cell edge in fast cell stretch and subsequent hold phases. In both cases, tip actin polymerization is augmented with strengthening cell edge stretch, which provides direct support for a force-velocity relationship of actin polymerization in cells, as originally predicted by the BR model (Peskin *et al.* 1993). The retrograde actin flow may contribute to this BR-based force sensing mechanism by enhancing the reactivity of actin polymerization to the force change. Conceptually, the BR mechanism can convert information on the location of a Brownian particle into energy (Astumian & Derenyi 1998), which has been shown experimentally (Serreli *et al.* 2007; Toyabe *et al.* 2010). For cells, the locally increased F-actin mass by stretch-induced tip polymerization may be regarded as biological information to guide cell protrusion and migration. We propose that tip actin barbed ends may serve as a BR-like sensor which converts the physical properties of outer environment to the local F-actin mass.

2 | RESULTS

2.1 | Substrate stretch instantaneously promotes actin assembly at the tip of lamellipodia

The response of the overall lamellipodial actin network to the stretch of the PDMS substrate is shown in Figure 1. XTC cells spreading on PLL-coated substrates extend wide lamellipodia (Watanabe & Mitchison 2002) and barely develop focal adhesions (Yamashiro & Watanabe 2014). The substrate was gradually displaced by using a manipulation needle stabbed into the PDMS substrate near the cell edge, and the stretched substrate was held for ≈3 min. Subsequently, tension was released. Upon stretch, an increase in the actin network was observed at the cell leading edge (Figure 1a; Figure S3; Movie 1 and 2). The bright actin network broadened from the tip to the base of lamellipodia at the speed of the retrograde actin flow (Figure 1b). Increased actin assembly at the cell edge was induced repeatedly by the stretch in cycles of stretch and tension release. Fluorescence intensity of EGFP-actin within 1 μm from the stretched cell edge was increased by 13.9%, 12.1% and 21.5% at 30 sec, 60 sec and 120 sec, respectively ($p < 0.05$, *t*-test) after initiation of cell stretch (Figure 1c).

We then employed SiMS microscopy to elucidate the effect of cell edge stretch on actin polymerization kinetics with high spatiotemporal resolution. The substrate was

displaced at a speed of up to 300 nm/s and the stretched substrate was held for ≈2 min. The extent of the stretch was quantified by the displacement of beads buried into the upper layer of the substrate. We found that outward stretch of the cell increased newly-emerged actin SiMS at the lamellipodium tip but not in the lamellipodium body (Figure 2a and 2b; Movie 3). Upon tension release, the appearance of new actin SiMS at the leading edge was decreased compared to before the stretch (Figure 2b).

We next focus on the initial reaction of actin assembly to the cell stretch manipulation. We found that the number of new actin SiMS was increased immediately upon cell stretch (Figure 3a). The increase in actin SiMS appearance (≈2-fold on average for 0~24 sec after initiation of stretch, Figure 3a) was much larger than the increase in EGFP-actin intensity near the cell edge (13.9% at 30 sec, Figure 1c). These data reveal that actin elongation is markedly accelerated at the stretched cell edge whereas the F-actin density is only marginally increased by the stretch. We further compared the relationship between the pulling speed and the actin SiMS appearance rate. We found that at the fast stretch step (0~24 sec after initiation of the stretch), the faster stretch speed was applied, the more actin SiMS newly appeared at the leading edge (Figure 3b). Augmentation of actin polymerization was significantly correlated with the stretch speed (Figure S4a). This relationship between SiMS appearance and the stretch speed was observed as early as 8

sec of the stretch (green dots in Figure 3b and Figure S4a). Importantly, the weighted average of new actin SiMS at the leading edge (columns in Figure 3b) indicates significant augmentation of tip actin polymerization in the fast stretch group (Figure S4b). The stretch manipulation led to transient slippage of actin SiMS toward the cell body with respect to the substrate (Figure 3c). The formation rate of the new actin network area, derived from the sum of the actin SiMS speed and the protrusion rate, was increased ≈1.3 folds upon stretch (Figure 3c). The network area formation rate was increased before slowing down of the retrograde actin flow and lasted until the tension was released (Figure 3c), suggesting that increased actin assembly, but not slowing down of the actin flow, promotes cell edge protrusion. Thus the data cannot be explained by a clutch model mechanism (Mitchison & Kirschner 1988), in which strengthening the coupling between actin and adhesion molecules slows the retrograde actin flow and thereby leads to cell edge protrusion under the assumption that the tip actin assembly rate remains constant.

2.2 │ Simulation based on a simple Brownian ratchet model recapitulates stretch-enhanced tip actin polymerization

The above relationship between tip actin polymerization and the stretch speed is reminiscent of the force-polymerization relationship in the BR models (Peskin *et al.* 1993;

Mogilner & Oster 1996, 2003): fast stretch speeds lead to large relative changes in actin polymerization rate, similar to the model by Peskin *et al*. (Peskin *et al.* 1993) that predicts an exponential dependence of velocity on force for single filaments. We therefore developed a physical model assuming a simple exponential dependence as in the Peskin *et al*. model. Force is generated by actin filaments in contact with the lamellipodium at various angles, the distribution of which was measured by using electron micrograph (Figure S5). We assumed that the viscosity of the cytosol and the slippage of the plasma membrane and the actin network over the substrate works as a 'damper' and the elasticity of the plasma membrane works as a 'spring' (see EXPERIMENTAL PROCEDURES for details of the model). The elastic force of the membrane is assumed to be constant during the stretch because cell stretch did not lead to an increase in the load on the tip actin barbed ends (See below; evidence is in Figure 5a). We premise that the 'damper' is a predominant mechanism for decreasing the load on the barbed end during fast stretch. The relationship predicted by our BR-based model (dotted line in Figure 3b) corresponds well with our results. These results reveal the BR mechanism operating at the lamellipodium tip.

Notably, during a cycle of stretch and release, the leading edge protruded beyond the initial position in accordance with the observed increased polymerization (Figure 4a),

supporting our notion that observed stretch-induced tip actin polymerization leads to cell protrusion. Figure 4b-e summarize the force-tip polymerization relationship and cell protrusion during the early phase of cell edge stretch. Deformation of the substrate stretches the cell periphery via interaction between the cell membrane and the substrate. This manipulation decreases the load to barbed ends in contact with the leading edge plasma membrane. Immediately tip actin polymerization increases at the cell edge. The increase in actin assembly with increasing stretch speeds is consistent with the exponential-like force-velocity relationship predicted by BR models. Promoted tip actin polymerization generates the protrusive activity. Membrane protrusion lasts on the tensioned substrates because of low loads on the barbed ends (See also below).

2.3 | Enhanced tip actin polymerization in stretch-to-hold phase is accompanied by reduced force on the tip actin barbed ends

The above data demonstrate the force-polymerization relationship supportive of a BR mechanism during fast stretch. In Figure 1b and 2b, however, enhanced tip actin polymerization continued during the hold step following the stretch. The ‘damper’ does not contribute to the force during this step. During hold, the ‘spring’ may not decrease the load on the barbed end compared to the initial condition. Therefore, there must be another

mechanism(s) by which tip actin polymerization is enhanced during the hold.

To estimate the load on the barbed end during the hold step following the stretch, we employed cytochalasin D. Treatment with a high dose of cytochalasin D rapidly inhibits elongation of cellular actin filaments (Forscher & Smith 1988; Higashida *et al.* 2004), leading to a loss of the actin-based pushing force for cell protrusion. Therefore, the extent of cell edge retraction induced by cytochalasin D reflects the load on the barbed end before the treatment. To accurately measure cell retraction, we monitored the contour of the plasma membrane (Smith *et al.* 2010) stained with PKH26. To our surprise, we found that the more the substrate was stretched, the less the leading edge retracted (Figure 5a and 5b; Movie 4 and 5). Retraction was reduced to less than one third of that observed in control cells by stretching the substrate over ≈5 μm (Figure 5b). These results indicate that the load on the actin barbed end is decreased in stretched cells (Figure 5c). In addition, these results suggest that elastic force of the plasma membrane does not increase upon stretch, which was assumed in our BR-based physical model (Figure 3b).

As PDMS get stretched, PDMS may become stiffer due to the increase in the instantaneous Young's modulus (Liu *et al.* 2009). The stiff substrate enhances cell spreading (Pelham & Wang 1997). We also noticed the improvement in cell spreading on the stretched substrate (Higashida *et al.* 2013). These observations imply that the

interaction between cell membrane and the substrate might be strengthened on the stiff substrate. The tensile force may change the conformation of the binding molecules, leading to the enhanced cell attachment. Thus the low load at the stretch and hold step (Figure 5b) is associated with enhanced actin polymerization at the cell edge (Figure 1b and 2b), which reveals another relationship compatible to the BR mechanism.

The dashed line in Figure 4a shows the estimated leading edge position based on the data on the actin polymerization rate and force predicted by comparison between the data in Figure 3b and 5b. The estimated leading edge position is roughly consistent with the observed position of the leading edge. Thus the force-tip polymerization relationships in early and hold steps of the stretch can account for the overall cell edge protrusion.

We further examined the force-tip polymerization relationship using pharmacological perturbation. We used 2,3-butanedione monoxime (BDM) (Higuchi & Takemori 1989), an inhibitor of skeletal muscle myosin-II and a blocker of the retrograde actin flow in lamellipodia. BDM attenuated actin assembly specifically at the lamellipodium tip. The dark region of EGFP-actin formed near the leading edge, and gradually expanded along the retrograde actin flow (Figure S6a and S6b; Movie 6). Upon washout of BDM, tip actin assembly was resumed and the dark band moved inward (Figure S6b). SiMS analysis revealed that the retrograde flow speed was reduced from ≈60 nm/s to ≈20 nm/s by 20

mM BDM, accompanied by a marked loss in the appearance of new actin SiMS at the leading edge (Figure S6c; Movie 7). The decrease in the appearance of actin SiMS was greater than the decrease in the actin flow speed. The reduction in the flow speed by BDM should increase the load onto the barbed end, thereby providing additional evidence of the force-polymerization relationship at the lamellipodium tip.

2.4 | Neither of the WAVE complex, Ena/VASP proteins are essential for stretch-induced tip actin polymerization

In addition, we examined the roles of actin regulators at the leading edge. First we tested the WAVE complex which activates the Arp2/3 complex (Machesky *et al.* 1999). In neutrophil, aspiration of the cell body by a micropipette delocalizes the WAVE complex from cell edge (Houk *et al.* 2012). This delocalization is attributed to the increase in the membrane tension. Knockdown of a WAVE complex constituent Nap1 (Eden *et al.* 2002) decreases the expression of other WAVE complex proteins (Kunda *et al.* 2003; Rogers *et al.* 2003; Steffen *et al.* 2004). We confirmed that EGFP-tagged WAVE2 and Sra-1 no longer localized to the leading edge in Nap1 knockdown cells (Figure S7 and S8a). These WAVE2 complex-depleted XTC cells formed somewhat shaggy lamellipodia with numerous filopodia. In these cells, stretch-induced tip actin polymerization was still

observed (Figure S8b and S9; Movie 8 and 9). Moreover, in these cells, BDM reduced the tip actin assembly which was rapidly resumed upon washout of BDM. (Figure S10; Movie 10). These observations were further confirmed in XTC cells overexpressing Abi1-mito (Maruoka *et al.* 2012), a high level expression of which depletes the WAVE complex from the leading edge (Figure S8c, S8d, S11 and S12; Movie 11-13). These results indicate that the WAVE2 complex is not essential for the stretch-induced tip actin polymerization.

Next we tested if Ena/VASP proteins mediate the stretch-induced tip actin polymerization. Localization of VASP at the leading edge increases with the protrusion rate (Rottner *et al.* 1999). VASP shields actin barbed ends from CapZ and promotes actin polymerization (Gertler *et al.* 1996; Bear *et al.* 2002). In the previous modeling studies on the force-velocity relation for *Listeria* (Mogilner & Oster 2003), VASP has been considered to act as a filament tether (Laurent *et al.* 1999) or a motor-like molecule fueled by ATP hydrolysis of actin (Dickinson & Purich 2002). We employed FP4-mito (Bear *et al.* 2000) to sequester Ena/VASP proteins on the mitochondrial surface (Figure S8e). In FP4-mito overexpressing cells, stretch-induced tip actin assembly was observed (Figure S8f and S13; Movie 14 and 15). The response to BDM was also retained in VASP-depleted cells (Figure S14; Movie 16). Thus, in response to stretch, cells lacking either

the WAVE complex or Ena/VASP proteins formed a dense actin network at the leading edge. Furthermore, the rapid enhancement of tip actin polymerization (<8 sec) (Figure 3b and Figure S4a) cannot be explained by the recruitment of the WAVE complex whose characteristic time is ≈30 sec after tension release of the plasma membrane (Houk *et al.* 2012).

2.5 │ Capping Protein and Formin homology proteins

We also found that lamellipodium tip-associated Capping Protein rapidly increases upon cell edge stretch (Figure S15). Thus uncapping of the actin barbed end is not the mechanism for stretch-induced tip actin polymerization. These results further support our hypothesis because traction force appears to promote intercalation of not only actin monomers but also Capping Protein between the actin barbed end and the plasma membrane. Involvement of formin homology proteins is not likely because EGFP-actin, which strongly suppresses the rate of processive actin elongation by formin homology proteins (Yamashiro *et al.* 2014) (Figure S16), is able to detect the stretch-induced tip actin assembly and subsequent cell edge protrusion (Figure 1 and Figure S3).

3 | DISCUSSION

Our study has thus revealed the two force-tip polymerization relationships at the mechanically stretched cell edge (Figure 4b-e and 5c). First, the rate of actin assembly at the cell edge increases with increasing stretch speed (Figure 3b and Figure S4). Second, at the hold step after the stretch, the displacement of the substrate decreases the load on the barbed ends (Figure 5b), which is accompanied by enhanced tip actin polymerization (Figure 2b). Neither the WAVE complex nor Ena/VASP proteins are essential in the stretch-induced tip actin polymerization. These relationships are in agreement with the force-velocity relationship predicted by the BR mechanism although the results do not distinguish among BR models predicting similar exponential force-velocity curves (Peskin *et al.* 1993; Mogilner & Oster 1996, 2003) and more complex models incorporating the BR force-velocity relationship (Carlsson 2003; Holz & Vavylonis 2018).

Our results are contradictory with the previous cell study showing increases in the density of actin network after loading force at the cell edge (Mueller *et al.* 2017). Our data do not fit with a concave force-velocity relationship at the lamellipodium tip (Prass *et al.* 2006; Heinemann *et al.* 2011; Zimmermann *et al.* 2012) either. In particular, the marked augmentation of polymerization in the fast stretch group (Figure S4b) cannot be explained by the concave relationship (Prass *et al.* 2006; Heinemann *et al.* 2011;

Zimmermann *et al.* 2012). This discrepancy might be attributable to the difference in the range of forces applied to the cell. Based on the maximal actin elongation rate, ≈81 subunits s^{-1} (Miyoshi *et al.* 2006), we predict that the load on the barbed end becomes ≈zero by the stretch faster than ≈210 nm/s (Figure 3b, dashed line). Our current study thus examined the force-polymerization relationship at normal to zero load on the barbed end. On the contrary, the previous cell studies focused on the maximum force generated by the lamellipodium tip when its forward movement was almost stalled against obstacles (Prass *et al.* 2006; Heinemann *et al.* 2011; Zimmermann *et al.* 2012). Real-time monitoring of actin SiMS is the key to our success in detecting the instantaneous reaction of tip actin polymerization when the force fluctuates within or below the normal range.

Also *in vitro*, distinct types of force-polymerization relationships such as a "dynamic stall", which is analogous to dynamic instability of microtubules, of small actin bundles (Footer *et al.* 2007) and an increase in the density and power of the dendritic actin network (Parekh *et al.* 2005; Bieling *et al.* 2016) have been observed. These properties are not necessarily contradictory with our findings in the present study. The properties of actin bundles (Footer *et al.* 2007) and the dendritic actin network (Parekh *et al.* 2005; Bieling *et al.* 2016) were examined when barbed-end growth was strongly restricted by forces, which is distinct from the *in vivo* situation where the retrograde actin flow can constantly

alleviate the physical constraint at the barbed end.

Almost all cultured cells growing on the culture substrate exhibit continuous retrograde actin flow at their periphery (Abercrombie *et al.* 1970) although its biological significance remains elusive. The retrograde flow is driven by an unknown flow-motor protein(s) in addition to the force generated by tip actin polymerization. The assist from putative flow-motors presumably elicits the force-polymerization relationship in favor of the "polymerization sensor". According to the force-polymerization relationship predicted by the BR models (Peskin *et al.* 1993; Mogilner & Oster 1996, 2003), the slope is steeper at a low force than at a high force (Figure 5d). The load decrease enhances actin polymerization more efficiently at barbed ends subject to low initial loads than high initial loads. Thus the retrograde actin flow renders barbed ends sensitive enough to exert stretch-induced enhanced polymerization by lowering the initial load. This enhanced polymerization corresponds to the extent of subsequent cell edge protrusion (Figure 4a).

Generation of force to push the cell edge membrane forward has been conceived to be the function of actin polymerization (Forscher & Smith 1988), which is referred to as the "polymerization motor" (Theriot 2000). We hereby propose that actin polymerization also serves as an active sensor for external force at the lamellipodium tip by utilizing the force-polymerization relationship of the BR mechanism. Our data (Figure 3a and 3b)

show that assembly of 5,700,000 actin subunits increased along the 20 μm-wide leading edge (roughly 1/8 of the cell edge) for 30 sec by stretching <5 μm, which exceeds 5 % of the total actin subunits in the cell (100 million subunits or less), leading to cell protrusion (Figure 4a). Thus actin polymerization functions as a 'sensor' of external force. We designate this function at the cell leading edge as a 'polymerization sensor'.

In theory, information can be converted into energy through the BR mechanism, which is referred to as 'information ratchet' (Astumian & Derenyi 1998). Information on the molecule's position drives the ratchet mechanism of the molecular ring (Serreli *et al.* 2007). Feedback manipulation of a Brownian particle on the basis of information about its location converts information to energy (Toyabe *et al.* 2010). In other words, the BR mechanism may serve as a converter between information and energy. Our data show that traction force controls actin monomer insertion in the manner predicted by the BR model. In our experiments, traction force was eventually converted to a locally extended F-actin mass, which can be regarded as storage of biological information to guide cell protrusion. We therefore propose that the role of the polymerization sensor is to collect information on the force exerted by the outer environment and store it in the form of the locally extended F-actin mass. The locally extended F-actin mass is then used as biological information for directed cell protrusion. Tip actin polymerization may be a unique BR-

based mechanism that constantly moves in one direction while efficiently sensing fluctuations of external forces for directing cell protrusion.

4 | EXPERIMENTAL PROCEDURES

4.1 | Plasmids and reagents

The expression vectors harboring the defective CMV promoter (delCMV) for EGFP-actin, EGFP-VASP, mCherry-actin, EGFP-CPβ1, EGFP-mDia1Full and EGFP-mDia1ΔN3 were described previously (Watanabe & Mitchison 2002; Miyoshi *et al.* 2006; Higashida *et al.* 2013; Yamashiro *et al.* 2014). *Xenopus laevis* WAVE2 cDNA was subcloned into pEGFP-C1 and mRFP1-C1. EGFP-Sra-1 (Steffen *et al.* 2004) and mRFP1-Abi1-mito (Maruoka *et al.* 2012) were described previously. The cDNA of FP4-mito from *Listeria* ActA (Bear *et al.* 2000) [a gift from Frank Gertler (MIT)] was subcloned into mRFP1-C1. Butandione monoxime (BDM) and cytochalasin D were purchased from Sigma.

4.2 | Cell culture and electroporation of fluorescent labeled actin

XTC cells were maintained and subjected to electroporation as described previously (Watanabe & Mitchison 2002; Yamashiro *et al.* 2014). Before electroporation, DL-actin in G-buffer (2 mM Tris-HCl pH 8.0, 0.1 mM $CaCl_2$, 0.2 mM ATP, 0.1% mercaptoethanol) was centrifuged at 346,000 g for 1 hour at 4 °C. Upper one half of the supernatant was collected. The supernatant (DL-actin, ≈5 μM) was mixed with 15 μM recombinant human

profilin1 in G-buffer and incubated for 1 hour on ice. Trypsinized XTC cells were resuspended in R buffer (Invitrogen) containing the DL-actin solution (DL-actin ≈0.75 μM, profilin ≈2.25 μM) at a density of 1.86×10^7 cells/ml. Two pulses (1005 V, 35 ms) were applied by the Neon transfection system (Invitrogen, Carlsbad, CA). Electroporated cells were washed 5 times with serum-free and riboflavin-free 70% Leibowitz L15 medium (Invitrogen) before seeding on the coverslips coated with PDMS.

4.3 | Cell membrane staining with PKH26

Cell membrane was stained with PKH26 Red Fluorescent Cell Linker (Sigma). XTC cells were dissociated by trypsinization and collected by centrifugation. The pellet was resuspended with 1 ml of 70% Leibowitz L15 medium (Invitrogen) without serum at a density of 2×10^6 cells/ml. The suspension was added to 1 ml of PKH26 solution (2×10^{-7} M final), and the solution was quickly mixed by pipetting. After incubation for 5 min, 2 ml of 70% Leibowitz L15 medium with 10% fetal calf serum was added to the suspension to stop the reaction. The cells were washed 3 times with 4 ml of 70% Leibowitz L15 medium with 10% fetal calf serum, and then resuspended with 70% Leibowitz L15 medium without serum before seeding on the PDMS-coated coverslips.

4.4 | RNA interference

The cDNA sequence of *Xenopus laevis* Nap1 was predicted from EST sequences (Accession numbers: DC116854, CF522709, BJ042100, CA787889, EB477047, BU907699, CA790064, BQ734063 and CD302059) with reference to the sequence of *Homo sapience* Nap1 (Accession number: NM_013436). The siRNAs targeting *Xenopus laevis* Nap1 (sense: 5'-GAAAGAACUUGCUACCGUAtt-3', antisense: 5'-UACGGUAGCAAGUUCUUUCaa-3', siRNA ID: s501411) were purchased from Ambion. We transfected plasmids into XTC cells using polyethylenimine (Watanabe 2012). Two days after transfection of plasmids, XTC cells were trypsinized and collected by centrifugation. Cells were resuspended at 2×10^7 cells/ml in R buffer containing 100 nM siRNA, and electroporated with three pulses of 1005 V for 35 ms using the Neon transfection system. We observed cells after 48~84 hours.

4.5 | Live cell imaging and SiMS microscopy on elastic substrate

The PDMS substrate was fabricated by using Sylgard 184 silicone elastomer kit (Dow Corning, Berry, UK). Sylgard 184 silicone elastomer base was mixed with curing agent at 19:1, and then degassed. Ethanol-washed round glass coverslips (Matsunami, No.0) were washed with H_2O five times and dried for 30 min at 100 °C. One hundred μl of

mixed PDMS was placed on the coverslip, and spin-coated using MS-A100 (Mikasa) at 3,000 rpm for 60 sec. Spin-coated PDMS was baked for 30 min at 100 °C. To overlay the upper layer, latex beads (0.8 μm diameter, Sigma) were mixed with the PDMS mixture at 10% by volume. The mixture (100 μl) was placed on the fabricated lower layer and spin-coated at 5,000 rpm for 60 sec. The coverslips were baked for 30 min at 100 °C. The PDMS surface was hydrophilized by exposing to plasma ion emitted from PIB-10 plasma ion bombarder (Vacuum Device, Ibaraki, Japan) at 6.5 mA for 30 sec (soft mode). The coverslips were floated on 200 μl of 1 mM sulfo-SANPAH (Thermo Scientific) coated-side down in 50 mM HEPES pH 8.5 and irradiated with UV light from UV transilluminator MUV21-365 (Major Science) for 30 min. The treatment with sulfo-SANPAH was repeated twice. Then the surface was washed five times with H_2O and incubated with poly-L-lysine (PLL, MW 150000-300000, Sigma) at RT overnight. PLL-coated PDMS was washed ten times with H_2O and treated with 1 ml of 10 mM Tris-HCl (pH 7.4) for 5 min, and then washed five times with H_2O.

SiMS imaging and live-cell imaging were performed as previously described (Watanabe 2012). Cells were observed on the stage of a microscope (IX71; Olympus) equipped with 100-W mercury, a EMCCD camera (iXon Ultra 897, Andor) and silicone immersion objective lens (UPLSAPO60XS2, NA 1.30, Olympus). PDMS coated

coverslips were mounted to Attofluor cell chamber (Invitrogen, A7816). XTC cells suspended with serum-free and riboflavin-free 70% L15 medium were seeded on the PDMS and incubated for 30 min before imaging. For manipulation experiments, a bent steel needle (27G × 1”, Terumo) was mounted to micromanipulator 5171 (Eppendorf) and stabbed into the PDMS substrate. The substrate was deformed by moving the stabbed needle horizontally. Images were acquired using the MetaMorph software (Molecular Devices).

4.6 ｜ Drug perfusion experiment

Drug perfusion was carried out as previously described (Watanabe 2012). XTC cells were spread on a glass coverslip (Matsunami, No.1) coated with PLL mounted on a custom flow cell (Watanabe 2012). Drug perfusion was carried out 30 min (up to 1 hour) after cell seeding. Observation was performed using a microscope (BX51, Olympus) equipped with a xenon lamp, a Cascade II:512 cooled charge-coupled device camera (Roper Scientific) and an oil-immersion objective lens (PlanApo×100 NA 1.40, Olympus).

4.7 ｜ TEM observation and analysis of the angle of actin filaments at the leading edge

Samples for transmission electron microscopy (TEM) were prepared according to the modified Auinger's methods (Auinger & Small 2008). We put the handmade negative grid mask using HF15 finder grid (Maxtaform No. G245) on the formvar-coated coverslip. Then the coverslips were coated with carbon using vacuum evaporator VE-2030 (Vacuum Device Inc.). The coverslips were glow-discharged using ion bombarder PIB-10 (Vacuum Device Inc.) before use. Then the coverslips were mounted to Attofluor cell chamber (Invitrogen, A7816) and coated with 10 μg/ml PLL at RT overnight. After washing with H_2O 20 times, cells were seeded on the chamber. After spreading, cells were permeabilized and fixed with 5% Triton X and 0.1% glutaraldehyde in cytoskeleton buffer for 5 sec according to previous method (Watanabe & Mitchison 2002). Then cells were washed with PBS including 500 mM NaCl 2 times and fixed with 2% glutaraldehyde in PBS. Fixed cells were remounted on the grid (Auinger & Small 2008). Samples were negatively stained with 2% phosphotungstic acid. Images of negatively stained cells were acquired by H7650 electron microscope (Hitachi) equipped with AMT XR-41C CCD camera system (Advanced Microscopy Techniques). To measure the filament angle, we used JFilament plugin of ImageJ (Smith *et al.* 2010). The angle was calculated from the slope of lines on the filament and the cell contour.

4.8 | Image analysis

To analyze single-molecule SiMS and the position of beads, we used Speckle TrackerJ plug-in (Smith *et al.* 2011) of ImageJ. JFilament plug-in (Smith *et al.* 2010) was used to detect the cell edge. The pseudo-color images were converted from grayscale images by using lookup tables “royal” in ImageJ.

We defined newly-emerged actin SiMS outside of preexisting actin SiMS as new actin SiMS at the leading edge. To normalize the density of actin SiMS in individual cells, we averaged new actin SiMS at the leading edge during -16~0 sec of stretch initiation. The average number was used for normalization of new actin SiMS in each time window (dots in Figure 3b). To derive the relationship between tip actin polymerization and stretch speed using the data from cells with various actin SiMS densities, we first let (i, j) be a set which satisfies $(k\text{-}1)\Delta v < y_{i,j} \leqq k\Delta v$ where $y_{i,j}$ represents the average speed of actin SiMS at time t_j in i-th cell. Here i = 1, 2, …, 8, j = 1, 2, …, 10, k = -4, -3, …, 1 and Δv = 60 (nm/sec). When k = -4, we calculated (i, j) which satisfies $y_{i,j} \leqq k\Delta v$. We then calculated the weighted averages N_k (columns in Figure 3b)

$$N_k = \frac{\sum_{ij} X_i x_{ij}}{\sum_i X_i}$$

where X_i represents the total number of new actin SiMS observed at the cell edge within -16~24 sec in i-th cell and x_{ij} represents the normalized number of new actin SiMS near

the leading edge (dots in Figure 3b).

4.9 | Physical modeling of force and polymerization relationship

To examine the consistency between the observed lamellipodial response to substrate stretch (Figure 3b) and the Brownian ratchet theory, we constructed a simple physical model which will be described in detail below.

In the present modeling, we focused on the response of leading edge against unidirectional substrate stretch and thus the model can be reduced to 1-dimension on which we describe the response of leading edge in the same direction as substrate stretch. Note that we defined all the model variables and parameters on the lab frame and took their signs the same as experimental data presentation. The velocity of lamellipodial tip v_l is given by the difference of the two opposing velocities, namely, membrane protrusion velocity v_p caused by actin polymerization and retraction velocity by actin retrograde flow v_r:

$$v_l = v_p + v_r \cdots (1).$$

Based on the Brownian ratchet mechanism (Mogilner & Oster 1996), we assumed that the protrusion velocity v_p exponentially changes to the total force f applied on the tip of a single actin filament pushing the membrane:

$$v_p = -v_a \cos\theta \exp\left[-\alpha f \cos\theta\right] \cdots (2)$$

where v_a is actin assembly velocity in the absence of load ($f = 0$) and θ represents the contact angle at which actin filaments push the membrane. The coefficient α in Eq. (2) is given by $\alpha = \delta/(k_B T)$ where δ represents the monomer size and $k_B T$ is thermal energy at temperature T. Substituting Eq. (2) into Eq. (1) and solving with respect to f gives

$$f(\theta) = -\frac{1}{\alpha \cos\theta} \ln\left(-\frac{v_l - v_r}{v_a \cos\theta}\right) \cdots (3).$$

For an arbitrary set of θ and v_l, we calculated the average force $\bar{f}$ as $\bar{f} = N \int P(\theta) f(\theta) d\theta$ where N is the total number of actin filament pushing the membrane and $P(\theta)$ represents the probability distribution of contact angle of actin filaments (Figure S5). Plotting v_p as a function of $\bar{f}$ yields the θ-averaged force-velocity curve. To transform the force-velocity curve into polymerization rate-stretch speed curve, we need to know the dependency of $\bar{f}$ on the substrate stretch speed v_s. Here we employed a phenomenological treatment where $\bar{f}$ is expressed as a Taylor series of v_s truncated by the first order like $\bar{f} = a v_s + b$. Note that this first order approximation means that force caused by substrate stretch is modeled as the sum of force $a v_s$ and constant force derived from elastic force of the plasma membrane b.

We assumed that elastic force of the membrane, which works like a ‘spring’, is

constant because the force does not appear to increase even when cells were stretched for more than >5 μm (Figure 5). av_s derives from the force between the substrate and the plama membrane and the force arising from the resistance of the actin network against stretch. The former force is generated by fast association and dissociation of electrostatically charged molecules between the substrate and the membrane, which pulls leading edge forward. The effect of this force can be monitored by the displacement of the beads because the displacement of the leading edge was approximately proportional to the beads displacement (with a 20% reduction, Figure 3c and 4a). As the leading edge is pulled, hydrostatic pressure is reduced and pulls cytosol through the actin network forward. We assume that the latter force is the friction between the cytosol and the actin network which is proportional to the speed of forward movement of the leading edge and works like a 'damper'. The sum of the former and the latter forces can therefore be regarded as proportional to v_s. The coefficients a and b were numerically determined in such a way that the point where $v_p = -v_r$ is satisfied in the force-velocity curve corresponds to the point at $v_s = 0$ in the polymerization rate-stretch speed curve. We also introduced another scaling factor to match the point where v_p reaches the maximum in the force-velocity curve to the point at $v_s = -220$ nm/s in the polymerization rate-stretch speed curve. About the model parameters, we set the value of v_a as 0.22 μm/s

(Miyoshi *et al.* 2006) and that of v_r as 0.1 μm/s based on our experiment (Figure 3c). The monomer size δ is 2.7 nm and $\delta/(k_BT) = 0.66$ pN^{-1} at room temperature. In the present study, we considered lamellipodia being 10 × 10 μm^2 wide and 0.16 μm high. The number of actin filaments N in contact with the 10 μm-wide leading edge plasma membrane was estimated to be 3000 by taking account for that the actin concentration in lamellipodia is ~1 mM (Abraham *et al.* 1999) and a 1 μm-long actin filament is composed of 360 subunits.

The cell edge protrusion in Figure 4a was estimated based on the data in Figure 3b and 5b by assuming that force reduction in Figure 5b gives rise to enhanced polymerization following the relationship verified in Figure 3b.

ACKNOWLEDGMENTS

We thank Frank B. Gertler (MIT) for FP4-mito cDNA and Orion Weiner (UCSF) for pEGFP-Sra-1. This work was supported by JST-CREST Grant Number JPMJCR15G5 (N.W.), by the Uehara Memorial Foundation (N.W.), by NIH R01 grant (R01GM114201) (D.V., N.W.), by a Grant-in-Aid for Scientific Research on Innovative Areas Grant Number 00624347 from the Ministry of Education, Science, Sports and Culture of Japan (S.Y.) and by JSPS KAKENHI Grant Number JP19H01020 (N.W.) and JP15K07045 (S.Y.).

CONFLICT OF INTERESTS

The authors declare no competing financial interests.

AUTHOR CONTRIBUTIONS

K.K. and N.W. designed experiments. K.K, S.Y., H.M. and N.W. performed experiments. K.K., D.T. S.Y. and N.W. analyzed data. D.T. and D.V. performed modeling analysis. K.K., D.T. D.V. and N.W. wrote the manuscript.

REFERENCES

Abercrombie, M., Heaysman, J.E. & Pegrum, S.M. (1970) The locomotion of fibroblasts in culture. 3. Movements of particles on the dorsal surface of the leading lamella. *Exp Cell Res* **62**, 389-398.

Abraham, V.C., Krishnamurthi, V., Taylor, D.L. & Lanni, F. (1999) The actin-based nanomachine at the leading edge of migrating cells. *Biophys J* **77**, 1721-1732.

Astumian, R.D. & Derenyi, I. (1998) Fluctuation driven transport and models of molecular motors and pumps. *Eur Biophys J* **27**, 474-489.

Auinger, S. & Small, J.V. (2008) Correlated Light and Electron Microscopy of the Cytoskeleton. *Methods Cell Biol* **88**, 257-272.

Bear, J.E., Loureiro, J.J., Libova, I., Fassler, R., Wehland, J. & Gertler, F.B. (2000) Negative regulation of fibroblast motility by Ena/VASP proteins. *Cell* **101**, 717-728.

Bear, J.E., Svitkina, T.M., Krause, M., Schafer, D.A., Loureiro, J.J., Strasser, G.A., Maly, I.V., Chaga, O.Y., Cooper, J.A., Borisy, G.G. & Gertler, F.B. (2002) Antagonism between Ena/VASP proteins and actin filament capping regulates fibroblast motility. *Cell* **109**, 509-521.

Bieling, P., Li, T.D., Weichsel, J., McGorty, R., Jreij, P., Huang, B., Fletcher, D.A. & Mullins, R.D. (2016) Force Feedback Controls Motor Activity and Mechanical Properties of Self-Assembling Branched Actin Networks. *Cell* **164**, 115-127.

Bray, D. (1984) Axonal growth in response to experimentally applied mechanical tension. *Dev Biol* **102**, 379-389.

Cai, Z., Qiu, W., Shao, G. & Wang, W. (2013) A new fabrication method for all-PDMS waveguides. *Sensors and Actuators A: Physical* **204**, 44-47.

Carlsson, A.E. (2003) Growth velocities of branched actin networks. *Biophys J* **84**, 2907-2918.

Demoulin, D., Carlier, M.F., Bibette, J. & Baudry, J. (2014) Power transduction of actin filaments ratcheting in vitro against a load. *Proc Natl Acad Sci U S A* **111**, 17845-17850.

Dickinson, R.B. & Purich, D.L. (2002) Clamped-filament elongation model for actin-based motors. *Biophys J* **82**, 605-617.

Eden, S., Rohatgi, R., Podtelejnikov, A.V., Mann, M. & Kirschner, M.W. (2002) Mechanism of regulation of WAVE1-induced actin nucleation by Rac1 and Nck. *Nature* **418**, 790-793.

Engler, A.J., Sen, S., Sweeney, H.L. & Discher, D.E. (2006) Matrix elasticity directs stem cell lineage specification. *Cell* **126**, 677-689.

Footer, M.J., Kerssemakers, J.W., Theriot, J.A. & Dogterom, M. (2007) Direct measurement of force generation by actin filament polymerization using an optical trap. *Proc Natl Acad Sci U S A* **104**, 2181-2186.

Forscher, P. & Smith, S.J. (1988) Actions of cytochalasins on the organization of actin filaments and microtubules in a neuronal growth cone. *J Cell Biol* **107**, 1505-1516.

Gertler, F.B., Niebuhr, K., Reinhard, M., Wehland, J. & Soriano, P. (1996) Mena, a relative of VASP and Drosophila Enabled, is implicated in the control of microfilament dynamics. *Cell* **87**, 227-239.

Heinemann, F., Doschke, H. & Radmacher, M. (2011) Keratocyte lamellipodial protrusion is characterized by a concave force-velocity relation. *Biophys J* **100**, 1420-1427.

Higashida, C., Kiuchi, T., Akiba, Y., Mizuno, H., Maruoka, M., Narumiya, S., Mizuno, K. & Watanabe, N. (2013) F- and G-actin homeostasis regulates mechanosensitive actin nucleation by formins. *Nat Cell Biol* **15**, 395-405.

Higashida, C., Miyoshi, T., Fujita, A., Oceguera-Yanez, F., Monypenny, J., Andou, Y., Narumiya, S. & Watanabe, N. (2004) Actin polymerization-driven molecular movement of mDia1 in living cells. *Science* **303**, 2007-2010.

Higuchi, H. & Takemori, S. (1989) Butanedione monoxime suppresses contraction and ATPase activity of rabbit skeletal muscle. *J Biochem* **105**, 638-643.

Holz, D. & Vavylonis, D. (2018) Building a dendritic actin filament network branch by branch: models of filament orientation pattern and force generation in lamellipodia. *Biophys Rev* **10**, 1577-1585.

Houk, A.R., Jilkine, A., Mejean, C.O., Boltyanskiy, R., Dufresne, E.R., Angenent, S.B., Altschuler, S.J., Wu, L.F. & Weiner, O.D. (2012) Membrane tension maintains cell polarity by confining signals to the leading edge during neutrophil migration. *Cell* **148**, 175-188.

Kunda, P., Craig, G., Dominguez, V. & Baum, B. (2003) Abi, Sra1, and Kette control the stability and localization of SCAR/WAVE to regulate the formation of actin-based protrusions. *Curr Biol* **13**, 1867-1875.

Lamoureux, P., Ruthel, G., Buxbaum, R.E. & Heidemann, S.R. (2002) Mechanical tension can specify axonal fate in hippocampal neurons. *J Cell Biol* **159**, 499-508.

Laurent, V., Loisel, T.P., Harbeck, B., Wehman, A., Grobe, L., Jockusch, B.M., Wehland, J., Gertler, F.B. & Carlier, M.F. (1999) Role of proteins of the Ena/VASP family in actin-based motility of Listeria monocytogenes. *J Cell Biol* **144**, 1245-1258.

Liu, M., Sun, J., Sun, Y., Bock, C. & Chen, Q. (2009) Thickness-dependent mechanical properties of polydimethylsiloxane membranes. *Journal of Micromechanics and*

Microengineering **19**, 035028.

Lo, C.M., Wang, H.B., Dembo, M. & Wang, Y.L. (2000) Cell movement is guided by the rigidity of the substrate. *Biophys J* **79**, 144-152.

Machesky, L.M., Mullins, R.D., Higgs, H.N., Kaiser, D.A., Blanchoin, L., May, R.C., Hall, M.E. & Pollard, T.D. (1999) Scar, a WASp-related protein, activates nucleation of actin filaments by the Arp2/3 complex. *Proc Natl Acad Sci U S A* **96**, 3739-3744.

Maruoka, M., Sato, M., Yuan, Y., Ichiba, M., Fujii, R., Ogawa, T., Ishida-Kitagawa, N., Takeya, T. & Watanabe, N. (2012) Abl-1-bridged tyrosine phosphorylation of VASP by Abelson kinase impairs association of VASP to focal adhesions and regulates leukaemic cell adhesion. *Biochem J* **441**, 889-899.

McGrath, J.L., Eungdamrong, N.J., Fisher, C.I., Peng, F., Mahadevan, L., Mitchison, T.J. & Kuo, S.C. (2003) The force-velocity relationship for the actin-based motility of Listeria monocytogenes. *Curr Biol* **13**, 329-332.

Mitchison, T. & Kirschner, M. (1988) Cytoskeletal dynamics and nerve growth. *Neuron* **1**, 761-772.

Miyoshi, T., Tsuji, T., Higashida, C., Hertzog, M., Fujita, A., Narumiya, S., Scita, G. & Watanabe, N. (2006) Actin turnover-dependent fast dissociation of capping protein in the dendritic nucleation actin network: evidence of frequent filament severing. *J Cell Biol* **175**, 947-955.

Mogilner, A. & Oster, G. (1996) Cell motility driven by actin polymerization. *Biophys J* **71**, 3030-3045.

Mogilner, A. & Oster, G. (2003) Force generation by actin polymerization II: The elastic ratchet and tethered filaments. *Biophys J* **84**, 1591-1605.

Mueller, J., Szep, G., Nemethova, M., de Vries, I., Lieber, A.D., Winkler, C., Kruse, K., Small, J.V., Schmeiser, C., Keren, K., Hauschild, R. & Sixt, M. (2017) Load Adaptation of Lamellipodial Actin Networks. *Cell* **171**, 188-200.

Parekh, S.H., Chaudhuri, O., Theriot, J.A. & Fletcher, D.A. (2005) Loading history determines the velocity of actin-network growth. *Nat Cell Biol* **7**, 1219-1223.

Pelham, R.J., Jr. & Wang, Y. (1997) Cell locomotion and focal adhesions are regulated by substrate flexibility. *Proc Natl Acad Sci U S A* **94**, 13661-13665.

Peskin, C.S., Odell, G.M. & Oster, G.F. (1993) Cellular motions and thermal fluctuations: the Brownian ratchet. *Biophys J* **65**, 316-324.

Prass, M., Jacobson, K., Mogilner, A. & Radmacher, M. (2006) Direct measurement of the lamellipodial protrusive force in a migrating cell. *J Cell Biol* **174**, 767-772.

Riveline, D., Zamir, E., Balaban, N.Q., Schwarz, U.S., Ishizaki, T., Narumiya, S., Kam, Z., Geiger, B. & Bershadsky, A.D. (2001) Focal contacts as mechanosensors:

externally applied local mechanical force induces growth of focal contacts by an mDia1-dependent and ROCK-independent mechanism. *J Cell Biol* **153**, 1175-1186.

Rogers, S.L., Wiedemann, U., Stuurman, N. & Vale, R.D. (2003) Molecular requirements for actin-based lamella formation in Drosophila S2 cells. *J Cell Biol* **162**, 1079-1088.

Rottner, K., Behrendt, B., Small, J.V. & Wehland, J. (1999) VASP dynamics during lamellipodia protrusion. *Nat Cell Biol* **1**, 321-322.

Serreli, V., Lee, C.F., Kay, E.R. & Leigh, D.A. (2007) A molecular information ratchet. *Nature* **445**, 523-527.

Smith, M.B., Karatekin, E., Gohlke, A., Mizuno, H., Watanabe, N. & Vavylonis, D. (2011) Interactive, computer-assisted tracking of speckle trajectories in fluorescence microscopy: application to actin polymerization and membrane fusion. *Biophys J* **101**, 1794-1804.

Smith, M.B., Li, H., Shen, T., Huang, X., Yusuf, E. & Vavylonis, D. (2010) Segmentation and tracking of cytoskeletal filaments using open active contours. *Cytoskeleton* **67**, 693-705.

Steffen, A., Rottner, K., Ehinger, J., Innocenti, M., Scita, G., Wehland, J. & Stradal, T.E. (2004) Sra-1 and Nap1 link Rac to actin assembly driving lamellipodia formation. *EMBO J* **23**, 749-759.

Theriot, J.A. (2000) The polymerization motor. *Traffic (Copenhagen, Denmark)* **1**, 19-28.

Toyabe, S., Sagawa, T., Ueda, M., Muneyuki, E. & Sano, M. (2010) Experimental demonstration of information-to-energy conversion and validation of the generalized Jarzynski equality. *Nature Physics* **6**, 988-992.

Watanabe, N. (2012) Fluorescence single-molecule imaging of actin turnover and regulatory mechanisms. *Methods Enzymol* **505**, 219-232.

Watanabe, N. & Mitchison, T.J. (2002) Single-molecule speckle analysis of actin filament turnover in lamellipodia. *Science* **295**, 1083-1086.

Watanabe, N., Tohyama, K. & Yamashiro, S. (2018) Mechanostress resistance involving formin homology proteins: G- and F-actin homeostasis-driven filament nucleation and helical polymerization-mediated actin polymer stabilization. *Biochem Biophys Res Commun* **506**, 323-329.

Wiesner, S., Helfer, E., Didry, D., Ducouret, G., Lafuma, F., Carlier, M.F. & Pantaloni, D. (2003) A biomimetic motility assay provides insight into the mechanism of actin-based motility. *J Cell Biol* **160**, 387-398.

Yamashiro, S., Mizuno, H., Smith, M.B., Ryan, G.L., Kiuchi, T., Vavylonis, D. & Watanabe, N. (2014) New single-molecule speckle microscopy reveals modification of the retrograde actin flow by focal adhesions at nanometer scales. *Mol Biol Cell* **25**,

1010-1024.

Yamashiro, S., Taniguchi, D., Tanaka, S., Kiuchi, T., Vavylonis, D. & Watanabe, N. (2019) Convection-Induced Biased Distribution of Actin Probes in Live Cells. *Biophys J* **116**, 142-150.

Yamashiro, S. & Watanabe, N. (2014) A new link between the retrograde actin flow and focal adhesions. *J Biochem* **156**, 239-248.

Yamashiro, S. & Watanabe, N. (2019) Quantitative high-precision imaging of myosin-dependent filamentous actin dynamics. *J Muscle Res Cell Motil.* published online https://doi.org/10.1007/s10974-019-09541-x

Zimmermann, J., Brunner, C., Enculescu, M., Goegler, M., Ehrlicher, A., Kas, J. & Falcke, M. (2012) Actin filament elasticity and retrograde flow shape the force-velocity relation of motile cells. *Biophys J* **102**, 287-295.

FIGUREURE LEGENDS

Figure 1

Increase in the density of the actin network at the lamellipodium edge upon stretch. (a) Images of an XTC cell expressing EGFP-actin before (left) and after (right) stretch are shown. Arrows indicate increases in the density of the actin network near the cell edge. Scale bars, 10 μm. (b) Images of EGFP-actin (top) and bright field (bottom) in the area indicated by the rectangle during cycles of the stretch and tension release manipulation are paneled at the interval of 10 sec. Note that upon stretch, the formation of a dense actin network is initiated at the lamellipodium tip (indicated by arrowheads), which gradually expands toward the cell center along the retrograde flow (see also Figure S3, Movie 1, 2). Scale bar, 5 μm. (c) Change in the EGFP-actin fluorescence intensity within 1 μm from the stretched cell edge. A significant increase was observed at 30 sec, 60 sec and 120 sec after initiation of stretch ($p < 0.05$, two-tailed *t*-test) but not after the release of stretch force at 300 sec. Mean ± s.d. is shown (n = 6).

Figure 2

Stretch-induced actin polymerization in lamellipodia. (a) Single-molecule speckles (SiMS) analysis of stretch-induced actin polymerization in lamellipodia (See also Movie

3). Blue lines indicate the cell edge. Scale bars, 10 μm. (b) Displacement of a bead buried into the PDMS substrate near the cell edge (top), the distance of the newly-emerged actin SiMS (middle) from the leading edge and their number at the leading edge (bottom) are shown. Note that the distance of new actin SiMS may not reflect the exact distance at its assembly because of their motion during image acquisition intervals and difficulty in determining the position of the leading edge.

Figure 3

Kinetics of stretch-induced actin polymerization at the lamellipodium tip. (a) Appearance of new actin SiMS at the stretched cell edge. The number of new actin SiMS normalized by the average between 16 sec and 0 sec before initiation of stretch in each cell (gray, n = 6) and its average (magenta) are shown. (b) The normalized number of new actin SiMS (n = 399) at the leading edge is plotted as a function of the stretch speed every 4 sec (8 cells). Blue, green and magenta dots indicate normalized number of new actin SiMS during hold (-16~0 sec), initial stretch (0~8 sec) and subsequent stretch (8~24 sec), respectively. Columns show the weighted average of the data binned at 60 nm/s intervals. The gray curve shows an exponential fit to the weighted average. The dashed curve shows the overall polymerization rate simulated by our Brownian ratchet-based model. The number of new actin SiMS is significantly correlated with the stretch speed. $p < 0.0001$

for all data, p = 0.012 for data between -16 sec and 8 sec (see also Figure S4a). (c) Comparison between actin SiMS kinetics and cell protrusion behavior during fast stretch and hold phases. The average and the data from 6 individual cells are shown in colored and gray lines, respectively. The top graph shows displacement of PDMS embedded beads near the stretched cell edge, which was used to estimate the speed of actin SiMS and the cell edge relative to the substrate (middle). The widening speed of the actin network at the cell edge was calculated by subtracting the leading edge speed from the speed of actin SiMS (bottom).

Figure 4

Summary of the polymerization sensor response to traction force. (a) Membrane protrusion induced by a cycle of stretch and tension release. Displacement of beads buried in the substrate (top) and position of the leading edge (bottom) are shown. The data from individual cells (n = 6) and their average are shown by gray and blue lines, respectively. The dashed line shows cell edge position estimated based on the data in Figure 3b and 5b by assuming that force reduction in Figure 5b gives rise to enhanced polymerization following the relationship in Figure 3b. The estimated cell edge position roughly corresponds with the observed cell edge behavior. (b) Summary of the initial response of tip actin polymerization during the fast stretch step. New actin filaments (light red)

assemble at the barbed end of the old actin filaments (dark red) against the force between the barbed end and the plasma membrane (the purple arrow). The actin filament flows inward with respect to the substrate. The surface of the PDMS substrate contains beads (green circles) for position reference. (c) The substrate is stretched by a stabbed manipulation needle (1). Upon stretch, the load to the end of actin filaments from the membrane presumably decreases (2). Simultaneously actin polymerization increases at the leading edge (3). During this initial stretch (green arrows), the cell edge retracts inward with respect to the substrate (blue dotted lines and blue arrows). Although the speed of the retrograde actin flow also increases with respect to the substrate (red dotted lines), the area of newly formed actin network (between blue arrows and red lines) was found to increase (Figure 3c). The density of new actin filaments also increases. Moreover, the faster the cell edge was stretched, the more actin polymerized at the cell edge in a manner predicted by the BR model (Figure 3b). (d) Promoted actin polymerization replenishes the protrusive activity in the late phase of stretch. (e) Actin polymerization continues to promote cell protrusion even after stretch is stopped (see also Figure 5).

Figure 5

Membrane retraction induced by cytochalasin D treatment was reduced on the tensioned substrate. (a) XTC cells stained with PKH26 were stretched to various extents and kept

in the hold phase for 40 sec before cytochalasin D treatment. Images of cells at 0 sec (red) and 100 sec (green) of 5 μM cytochalasin D treatment on the substrate without tension (top) and with tension (bottom) are shown. Scale bar, 10 μm. (b) Retraction of the leading edge 100 sec after 5 μM cytochalasin D. The average retraction distance of the leading edge with respect to the substrate was measured in the range of center angle of ±11.25° from the stretch axis. Orange dots show the data from individual cells (n = 21). The line shows an exponential curve fit with the data. The P-value of Pearson's correlation coefficient (r = -0.643, two-tailed) is shown on the graph. (c) Summary of the force-polymerization relationship on the tensioned substrate. Sustained substrate stretch augments tip actin polymerization, concomitantly decreasing the force on the barbed end as evidenced by the data in Figure 1b, 2b and 4a. Stiffening of the substrate by the stretch may thus assist cell adhesion and reduce the load on the lamellipodium tip actin barbed end. (d) Retrograde flow-assisted BR-based actin polymerization sensor model. The curve shows the force-polymerization relationship for a single filament predicted by the Brownian ratchet mechanism (Peskin *et al.* 1993). The continuous retrograde actin flow in lamellipodia keeps the initial load on the barbed end small. In the "flow-assisted" situation, the rate of tip actin polymerization is greatly enhanced by traction forces (Figure 3b), leading to gradual cell protrusion (Figure 4a). In contrast, the case "with minimum

flow-assist" cannot yield biologically meaningful protrusion. Red and blue dashed lines indicate the range considering typical filament angles in lamellipodia (Figure S5). The shaded area indicates the range of the actin flow speed in XTC cells.

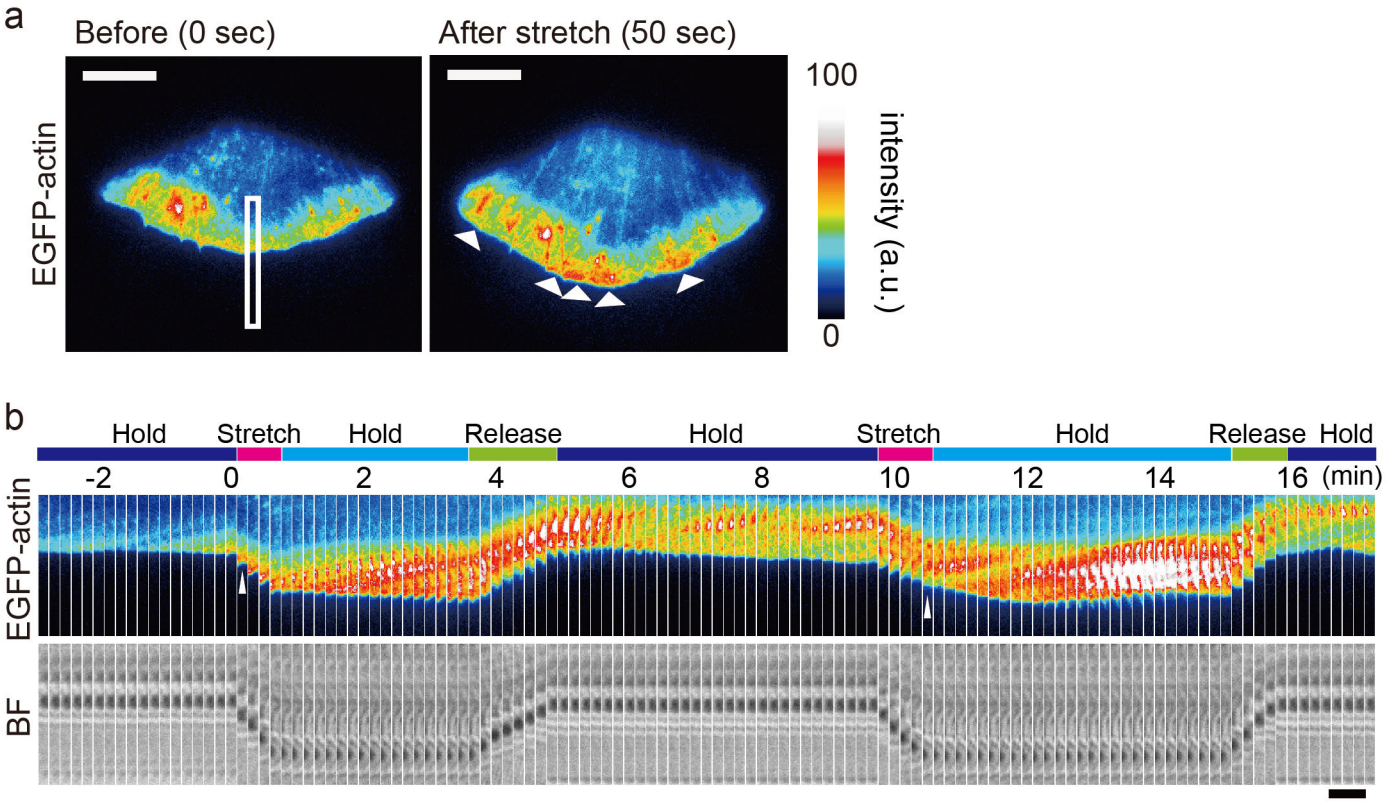
a
Before (0 sec)
After stretch (50 sec)
EGFP-actin
100
intensity (a.u.)
0
b
Hold
Stretch
Hold
Release
Hold
Stretch
Hold
Release
Hold
-2
0
2
4
6
8
10
12
14
16
(min)
EGFP-actin
BF
c
Increase in EGFP-actin fluorescence within 1 micron from the edge
1.4
1.2
1
0.8
0.6
0.4
0.2
0
before
30
60
120
300
Time after initiation of stretch (sec)

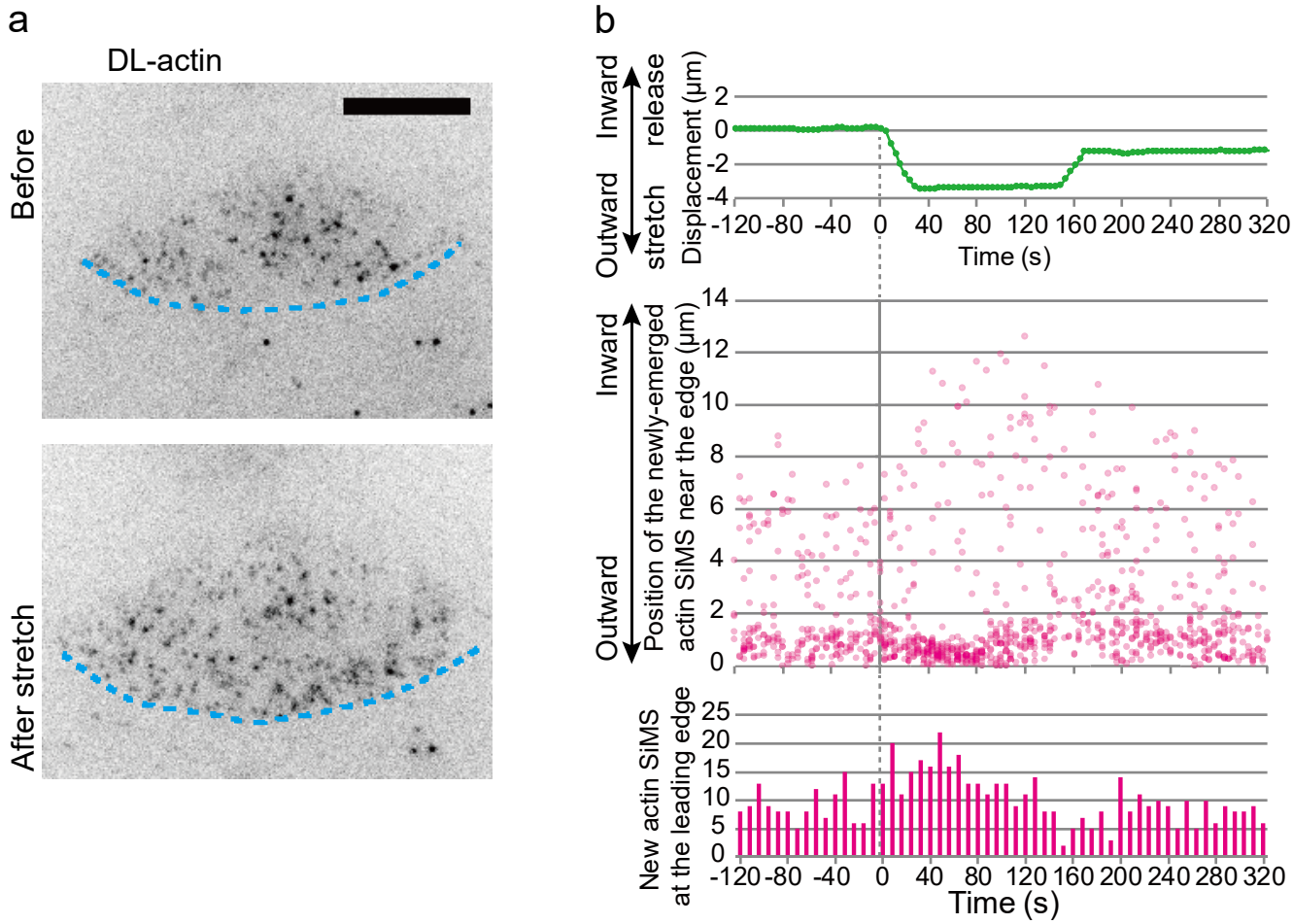
a
DL-actin
Before
After stretch
b
Inward
release
Outward
stretch
Displacement (μm)
2
0
-2
-4
-120 -80 -40 0 40 80 120 160 200 240 280 320
Time (s)
Inward
Outward
Position of the newly-emerged actin SiMS near the edge (μm)
14
12
10
8
6
4
2
0
New actin SiMS at the leading edge
25
20
15
10
5
0
-120 -80 -40 0 40 80 120 160 200 240 280 320
Time (s)

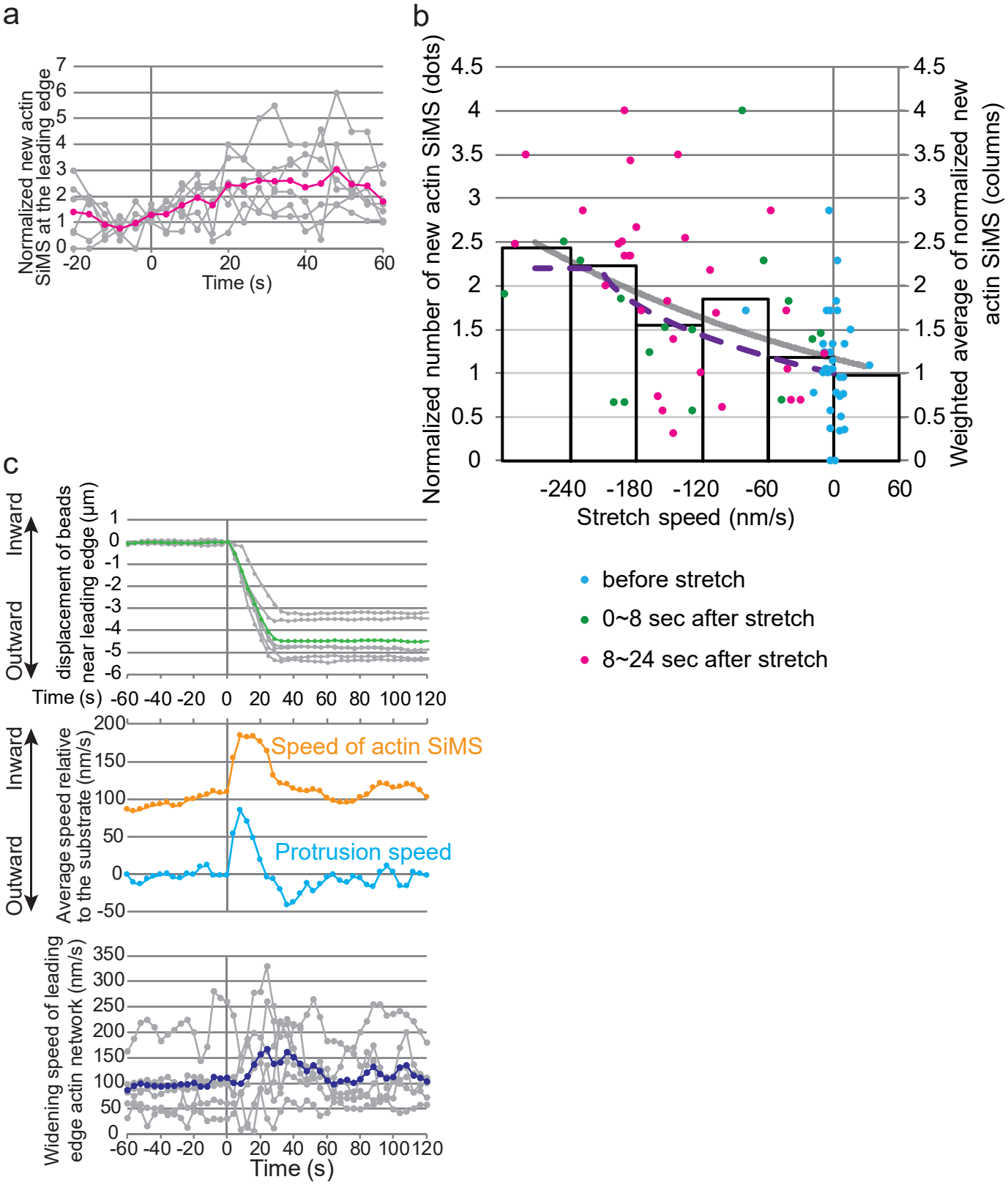
a
Normalized new actin SiMS at the leading edge
Time (s)
b
Normalized number of new actin SiMS (dots)
Weighted average of normalized new actin SiMS (columns)
Stretch speed (nm/s)
before stretch
0~8 sec after stretch
8~24 sec after stretch
c
Inward
Outward
displacement of beads near leading edge (μm)
Time (s)
Speed of actin SiMS
Protrusion speed
Average speed relative to the substrate (nm/s)
Widening speed of leading edge actin network (nm/s)
Time (s)

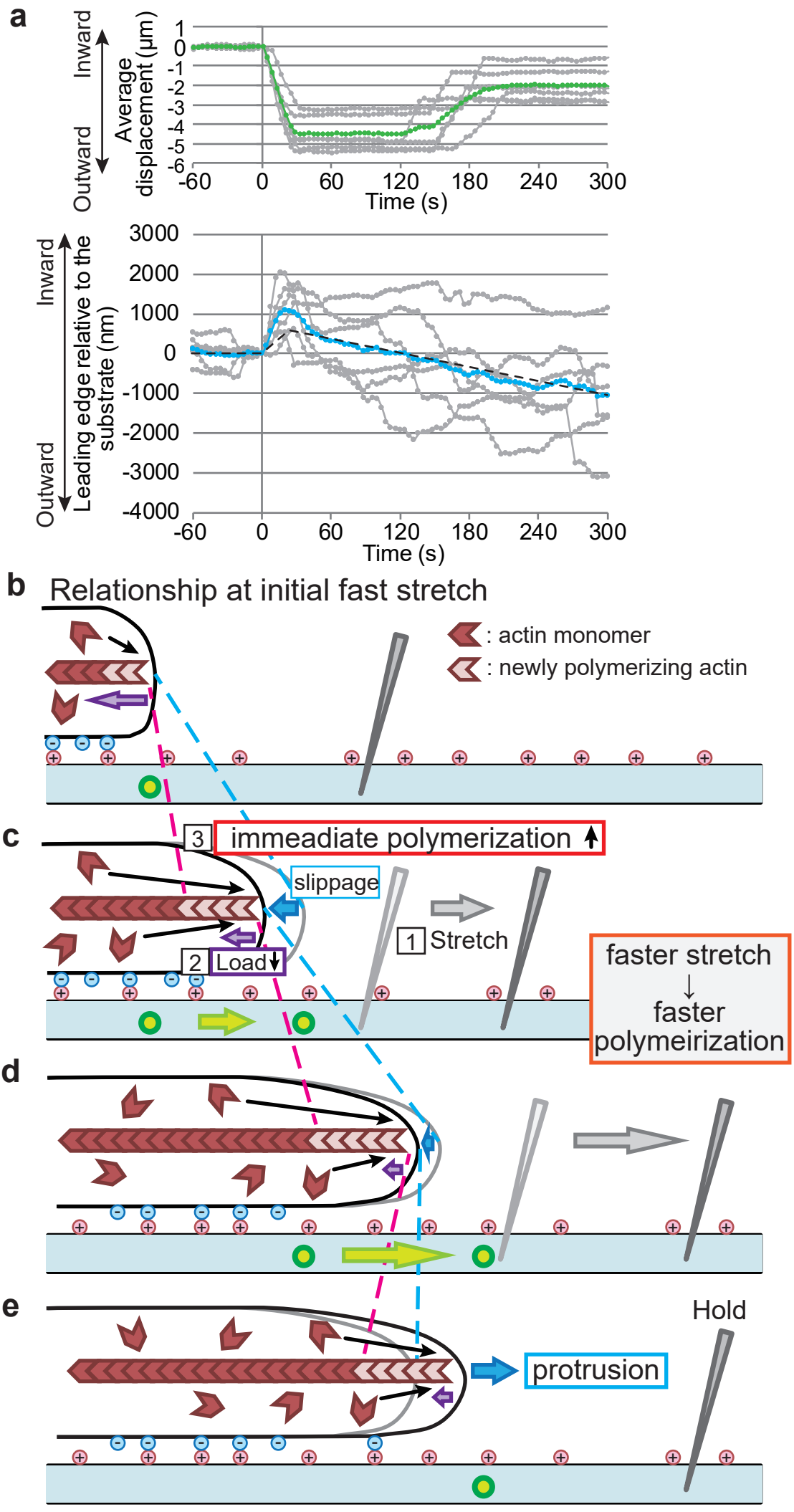
a
Inward
Outward
Average displacement (μm)
1
0
-1
-2
-3
-4
-5
-6
-60
0
60
120
180
240
300
Time (s)
Inward
Outward
Leading edge relative to the substrate (nm)
3000
2000
1000
0
-1000
-2000
-3000
-4000
-60
0
60
120
180
240
300
Time (s)
b
Relationship at initial fast stretch
: actin monomer
: newly polymerizing actin
c
3
immeadiate polymerization
slippage
1
Stretch
2
Load
faster stretch
↓
faster
polymeirization
d
e
Hold
protrusion

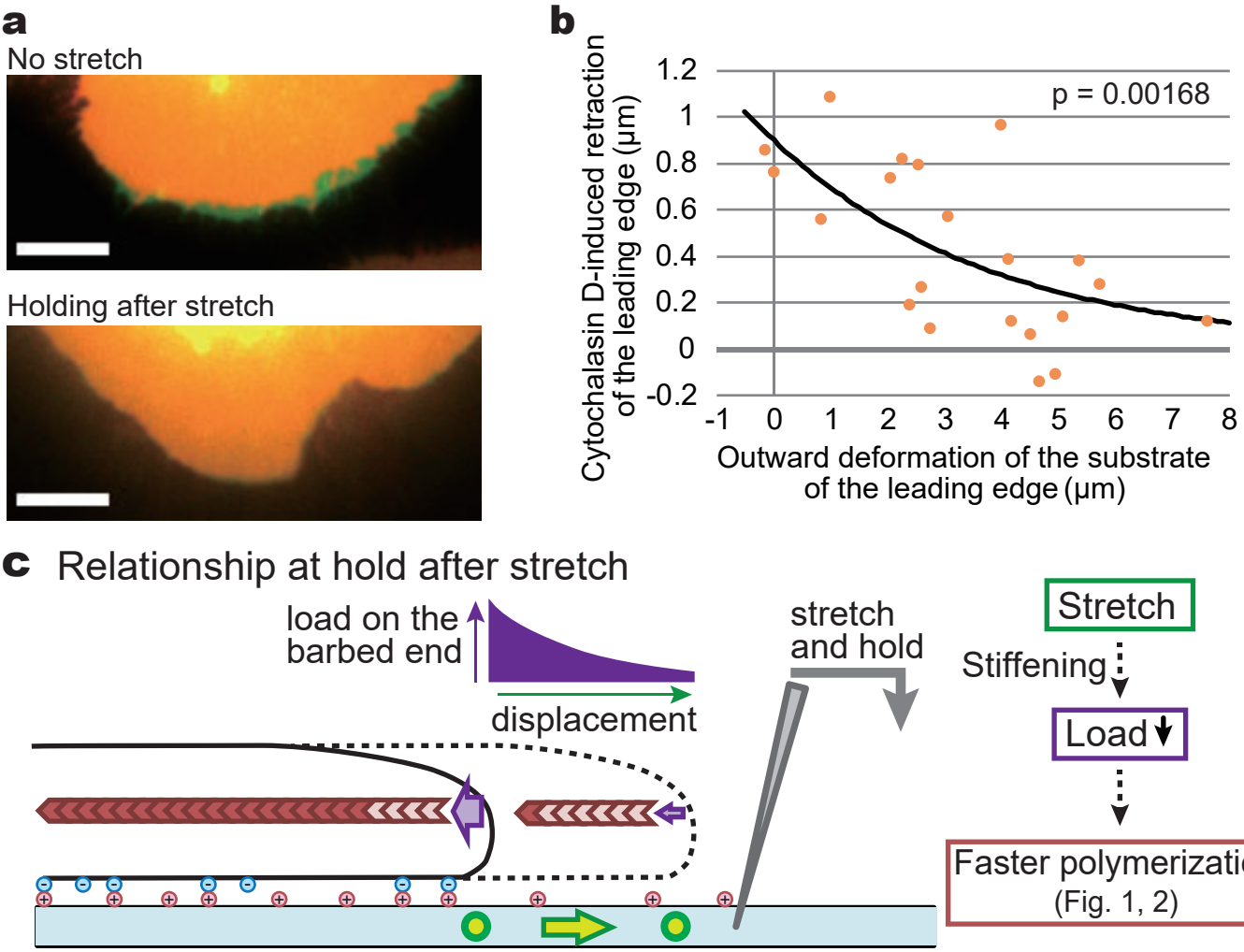
a
No stretch
Holding after stretch
b
p = 0.00168
Cytochalasin D-induced retraction of the leading edge (μm)
Outward deformation of the substrate of the leading edge (μm)
c Relationship at hold after stretch
load on the barbed end
displacement
stretch and hold
Stretch
Stiffening
Load
Faster polymerization
(Fig. 1, 2)
d Model for retrograde flow-assisted, BR ratchet-based force sensor
flow-assisted
ΔLoad = -0.5
Δv = ≈50
with minimum flow-assist
ΔLoad = -0.5
Δv = ≈7
v (polymerization rate; nm/s)
Load on the F-actin barbed end (a.u.)

Supplementary Information for

Lamellipodium tip actin barbed ends serve as a force sensor

Supplementary Figure S1-S16

Movie captions

Figure S1

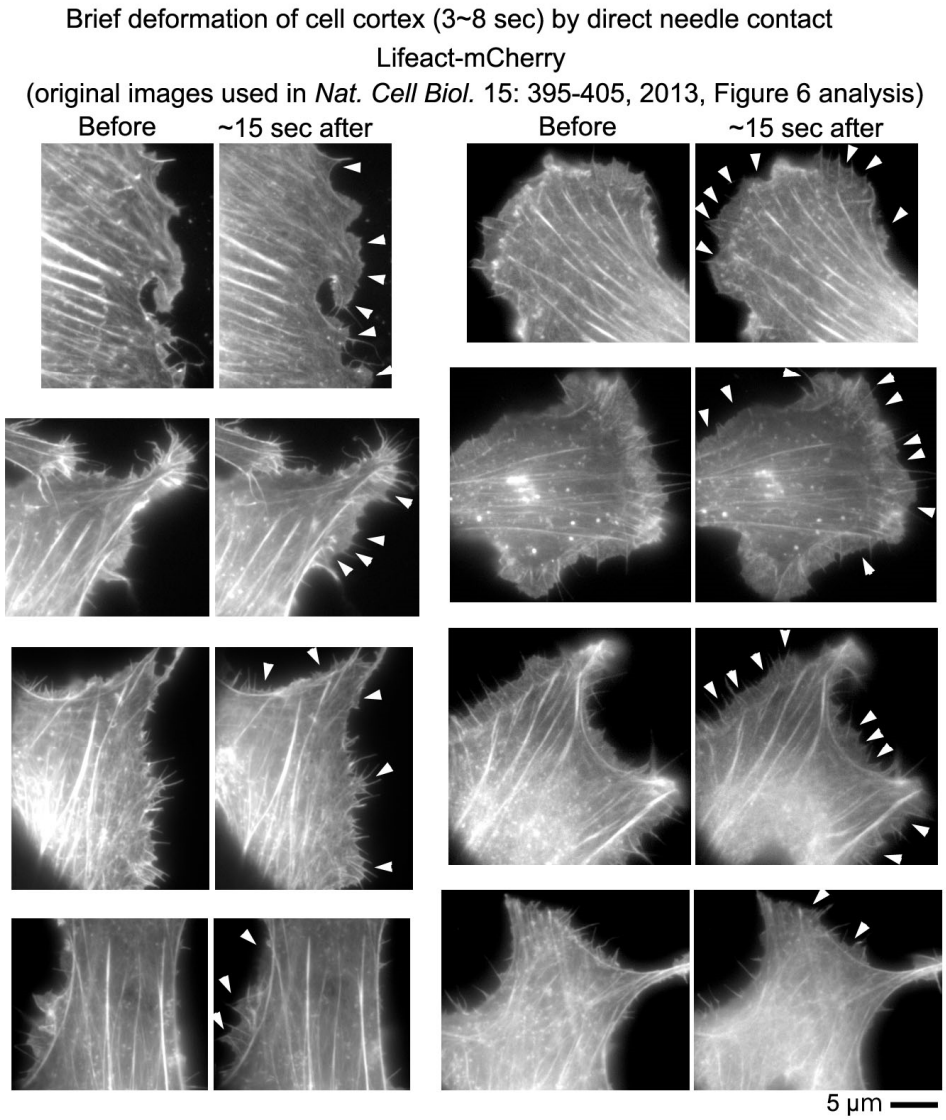

Brief deformation of the perinuclear cell cortex attenuates actin assembly in lamellipodia. In this experiment, a glass microneedle was placed on the cell surface by using a micromanipulator. The cell cortex near the nucleus was displaced laterally for 4~7 μm and transiently for 3~8 sec, and the tension was released. The images show F-Actin distribution visualized by Lifeact-mCherry before and ≈15 s after needle manipulation. These data were originally used in our previous study (Figure 6a-c in *Nat. Cell Biol*. 15, 395-405, 2013). Eight cell examples which had apparent lamellipodia are shown out of 16 cell data. The decrease in the F-actin density in lamellipodia was observed (arrowheads on the right images) all over the cell periphery regardless of the direction of cell cortex deformation.

Figure S2

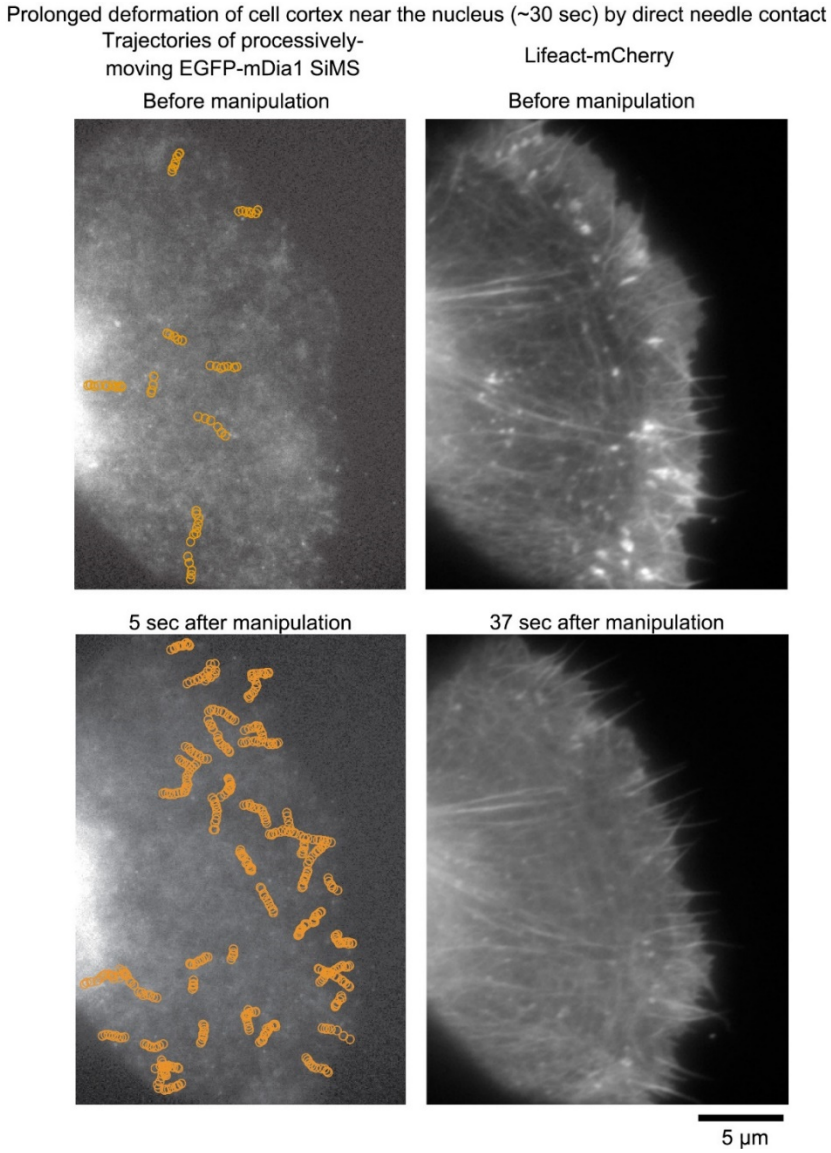

Prolonged deformation (~30 sec) of the perinuclear cell cortex reduced F-actin density in lamellipodia. The micromanipulation procedure was the same as in Figure S1 except that cell cortex was displaced for longer duration (~30 sec). Trajectories of directionally-moving wild-type mDia1 (EGFP-tagged, visualized at the single-molecule imaging level) are shown by orange circles on the left. F-actin visualized by Lifeact-mCherry before and 37 sec after needle manipulation are shown on the right. Note the marked F-actin decrease in lamellipodia and its increase in the lamella region, which is attributable to massively enhanced activities of formin homology proteins (see also the data for other formins in *Nat. Cell Biol.* 15, 395-405, 2013). These results (Figure S1 and S2) prompted us to avoid the use of microneedles and pipettes directly in contact with the cell surface to apply the force to the lamellipodium tip in the present study.

Figure S3

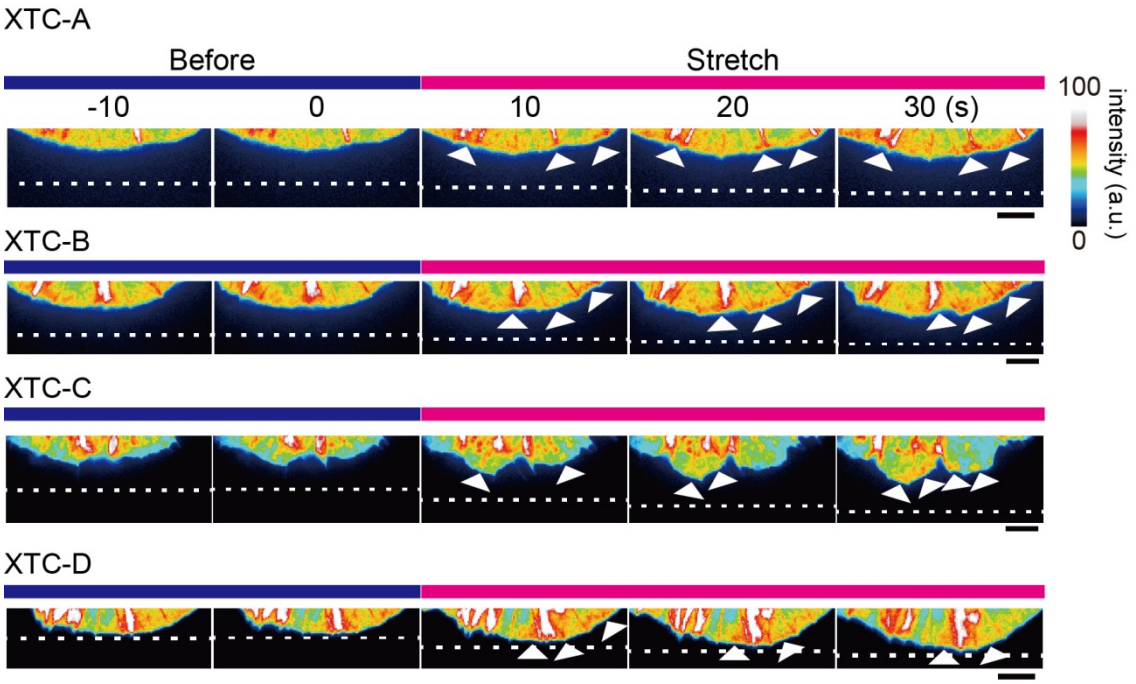

The increase in the density of the actin network at the leading edge upon stretch (other examples of Figure 1 experiments)

Time lapse images of GFP from the four XTC cells expressing EGFP-actin are shown. White lines indicate the vertical position of the center of a bead buried into the PDMS substrate. Time is the same as shown on the top of XTC-A images. Arrowheads indicate lamellipodium tip areas associated with enhanced EGFP-actin signals. Scale bars, 5 μm.

Figure S4

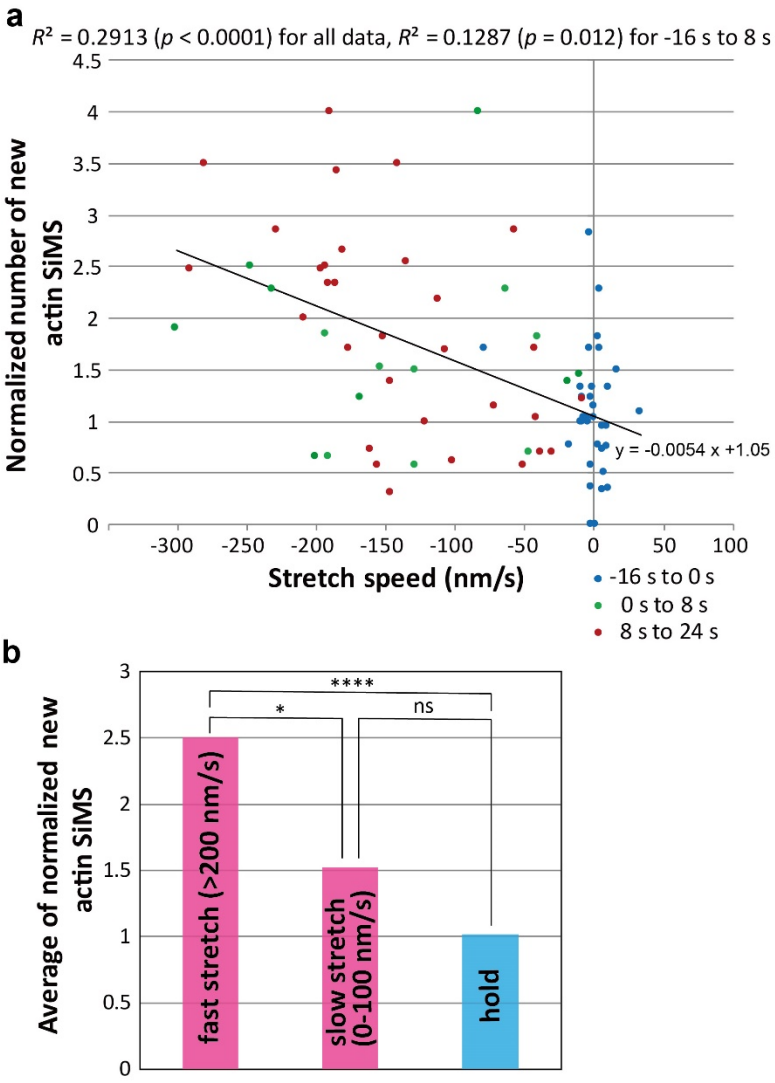

Statistical analysis of Figure 3b data

(**a**) Correlation between the stretch speed and the normalized number of new actin SiMS at the lamellipodium tip (n = 80 data points; 8 cells and 399 actin SiMS). The P-values on the top of the graph were calculated using Pearson's correlation coefficient (two-tailed). (**b**) Comparison of the normalized numbers of new actin SiMS between hold (-16 s to 0 s from the initiation of substrate stretch, indicated by blue dots in Figure 3b and Figure S3a), slow stretch (0 - 100 nm/s) and fast stretch (> 200 nm/s). * $p < 0.05$, **** $p < 0.0001$, ns: not significant (Mann-Whitney test).

Figure S5

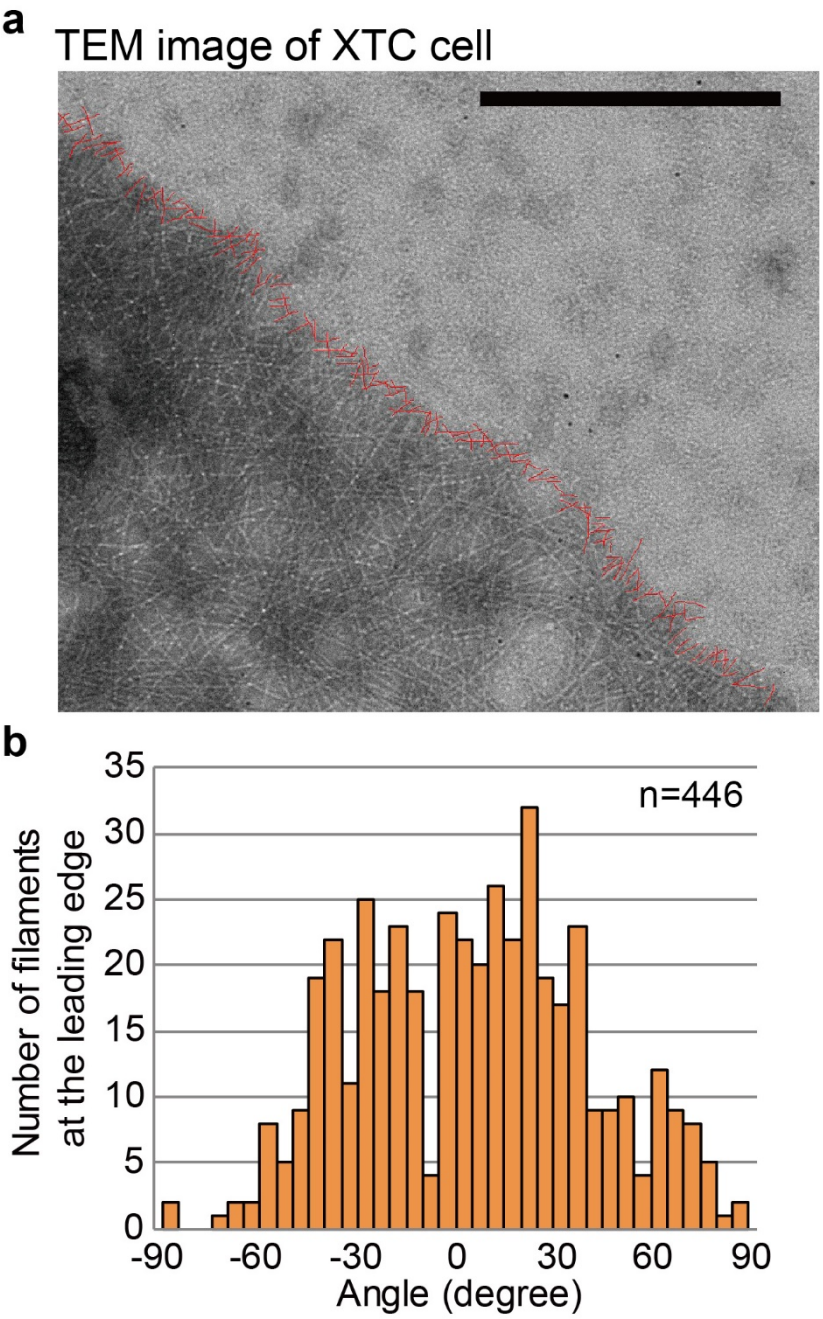

Orientation distribution of actin filaments at the leading edge

(**a**) A TEM image of an XTC cell is shown. Scale bar, 500 nm. (**b**) Orientation distribution of actin filaments at the leading edge is shown. We measured the orientations of filaments at the edges with respect to the perpendicular line relative to the membrane in 3 cells (n = 446).

Figure S6

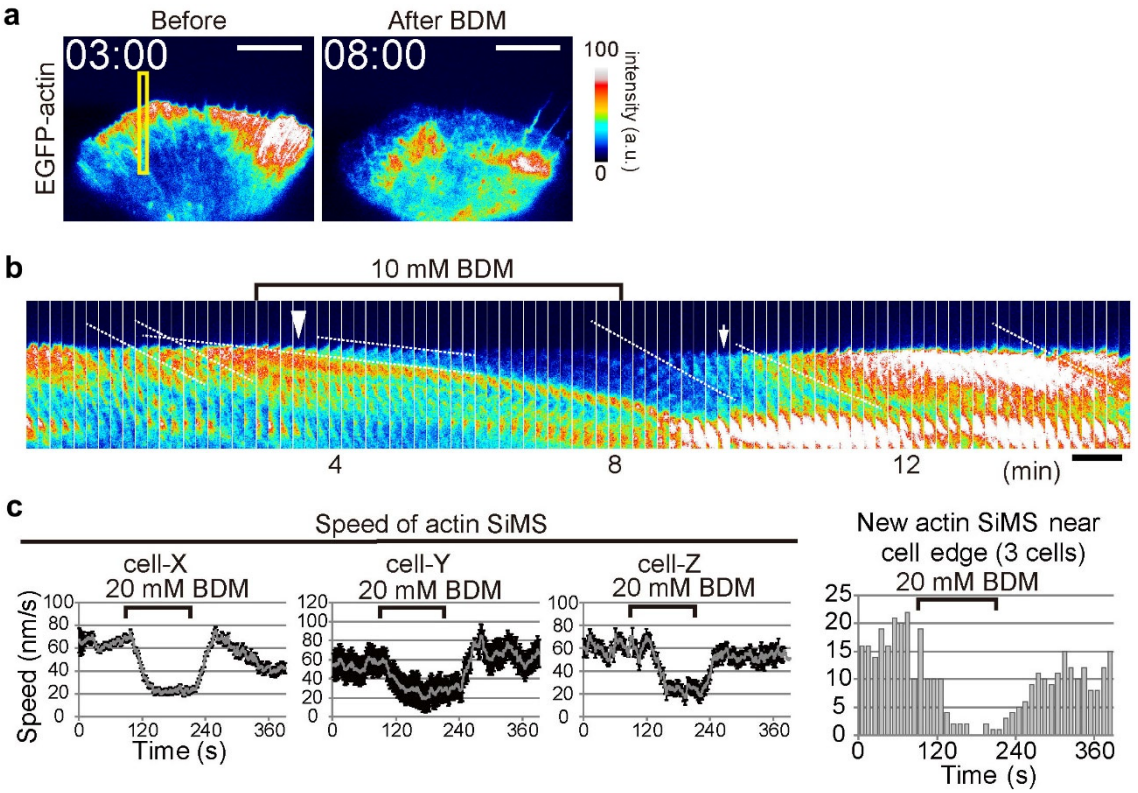

Reduction of tip actin polymerization upon inhibition of the retrograde actin flow

(**a**) BDM treatment attenuates actin assembly at the lamellipodium tip. EGFP-actin in XTC cell spreading on a PLL-coated glass coverslip before (left) and 5 min after treatment with 10 mM BDM (right) are shown. Scale bars, 10 μm. (**b**) Images in the rectangle in A are paneled at the interval of 10 sec. Dashed lines indicate the actin retrograde flow. Accompanied by the actin flow deceleration, newly emerged EGFP-actin was markedly decreased at the cell edge (arrowhead). After wash out of BDM, bright EGFP-actin label was recovered from the cell edge (arrow). Scale bar, 5 μm. (**c**) The BDM-induced decrease in actin assembly was greater than the decrease in the flow speed. The average and the standard deviation of the actin retrograde flow speed are shown in gray and black, respectively. On the right, the summed number of newly appeared actin SiMS near the edge of cells X-Z is shown.

Figure S7

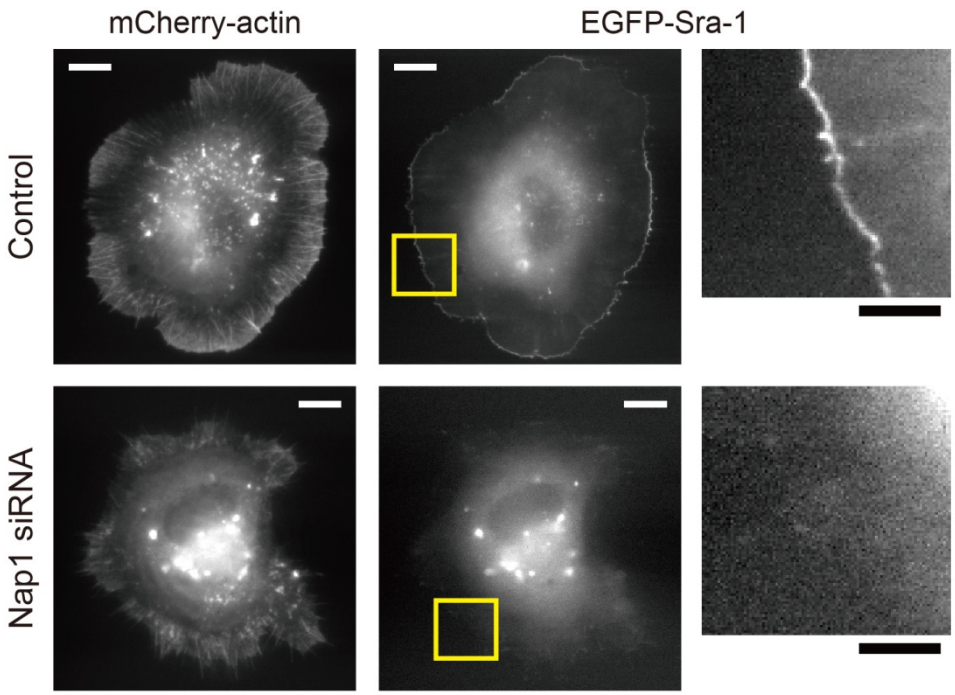

Mislocalization of Sra-1 from the leading edge in Nap1-depleted cells

Images of control cell (top) and Nap1-depleted cell (bottom) expressing EGFP-actin and EGFP-Sra-1 are shown. Boxed regions in the images of EGFP-Sra-1 are shown in the right of original images. Scale bars, 10 μm.

Figure S8

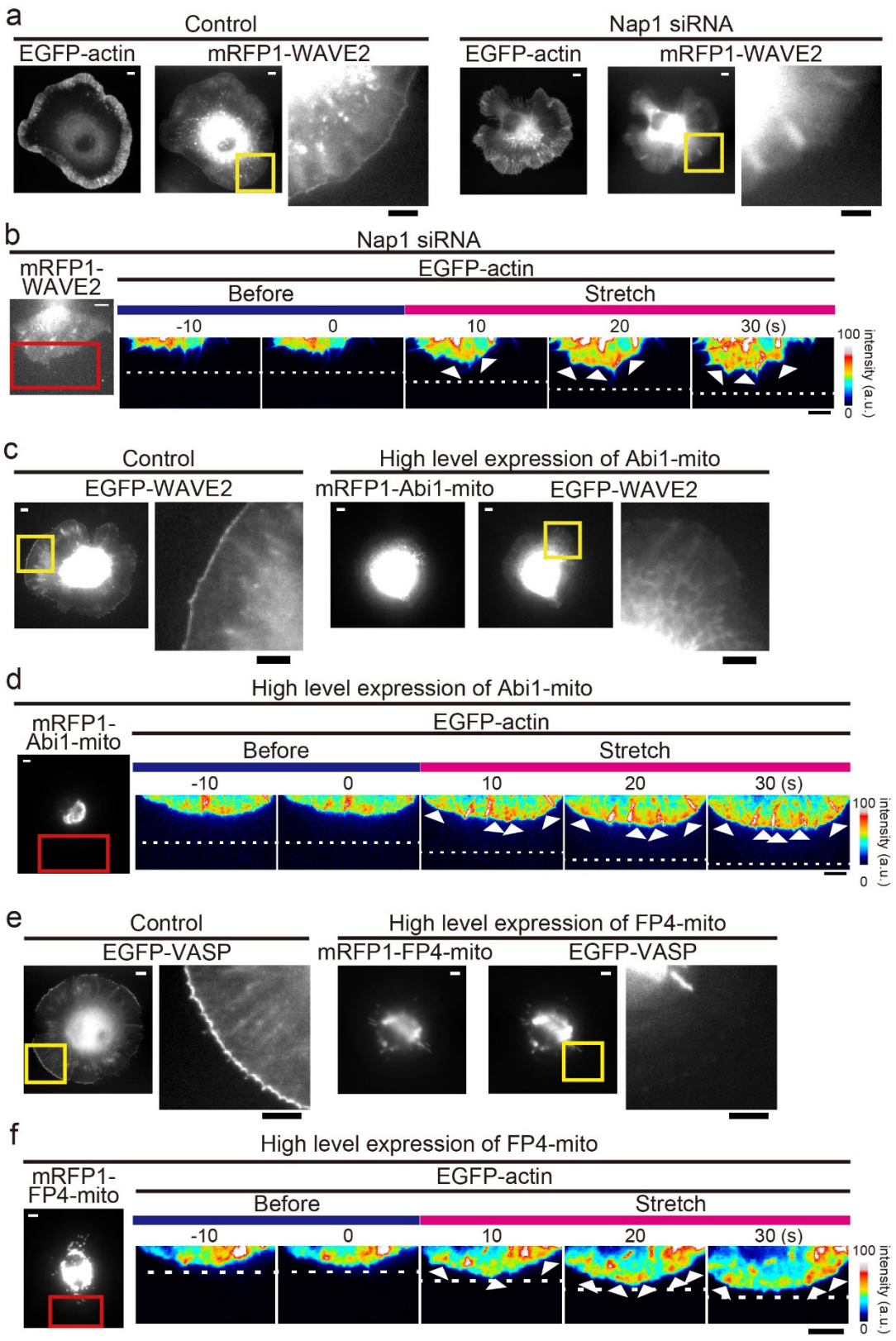
a
Control
Nap1 siRNA
EGFP-actin
mRFP1-WAVE2
EGFP-actin
mRFP1-WAVE2
b
Nap1 siRNA
mRFP1-WAVE2
EGFP-actin
Before
Stretch
-10
0
10
20
30 (s)
100
intensity (a.u.)
0
c
Control
High level expression of Abi1-mito
EGFP-WAVE2
mRFP1-Abi1-mito
EGFP-WAVE2
d
High level expression of Abi1-mito
mRFP1-Abi1-mito
EGFP-actin
Before
Stretch
-10
0
10
20
30 (s)
100
intensity (a.u.)
0
e
Control
High level expression of FP4-mito
EGFP-VASP
mRFP1-FP4-mito
EGFP-VASP
f
High level expression of FP4-mito
mRFP1-FP4-mito
EGFP-actin
Before
Stretch
-10
0
10
20
30 (s)
100
intensity (a.u.)
0

Stretch-induced tip actin polymerization is not blocked by the depletion of either the WAVE complex or Ena/VASP proteins

(**a**) Nap1 was depleted by RNAi in XTC cells expressing EGFP-actin and mRFP1-WAVE2. Boxed regions are enlarged on the right, showing the loss of WAVE2 at the lamellipodium tip by Nap1 knockdown. (**b**) Time lapse images of EGFP-actin in a rectangle in the image of mRFP1-WAVE2 (left) were paneled at the interval of 10 sec. Dotted lines indicate the positions of a bead buried into the substrate. Arrowheads indicate lamellipodium tip areas associated with enhanced EGFP-actin signals. See also Figure S9 for other examples. (**c**) Depletion of the WAVE complex from the cell edge in cells overexpressing mRFP1-Abi1-mito. Boxed regions are enlarged on the right, showing sequestration of WAVE2 on mitochondria in the Abi1-mito expressing cell. (**d**) Images of EGFP-actin in the rectangle (left) are paneled at the interval of 10 sec. Dotted lines indicate the positions of a bead buried into the substrate. Arrowheads indicate lamellipodium tip areas associated with enhanced EGFP-actin signals. See also Figure S11 for other examples. (**e**) Ena/VASP proteins were depleted from the cell edge in XTC cells expressing a high level of FP4-mito. Boxed regions were enlarged on the right. (**f**) Images of EGFP-actin in the rectangle (left) are paneled at the interval of 10 sec. Dotted lines indicate the position of a bead buried into the substrate. Arrowheads indicate lamellipodium tip areas associated with enhanced EGFP-actin signals. See also Figure S13 for other examples. Scale bars, 5 μm.

Figure S9

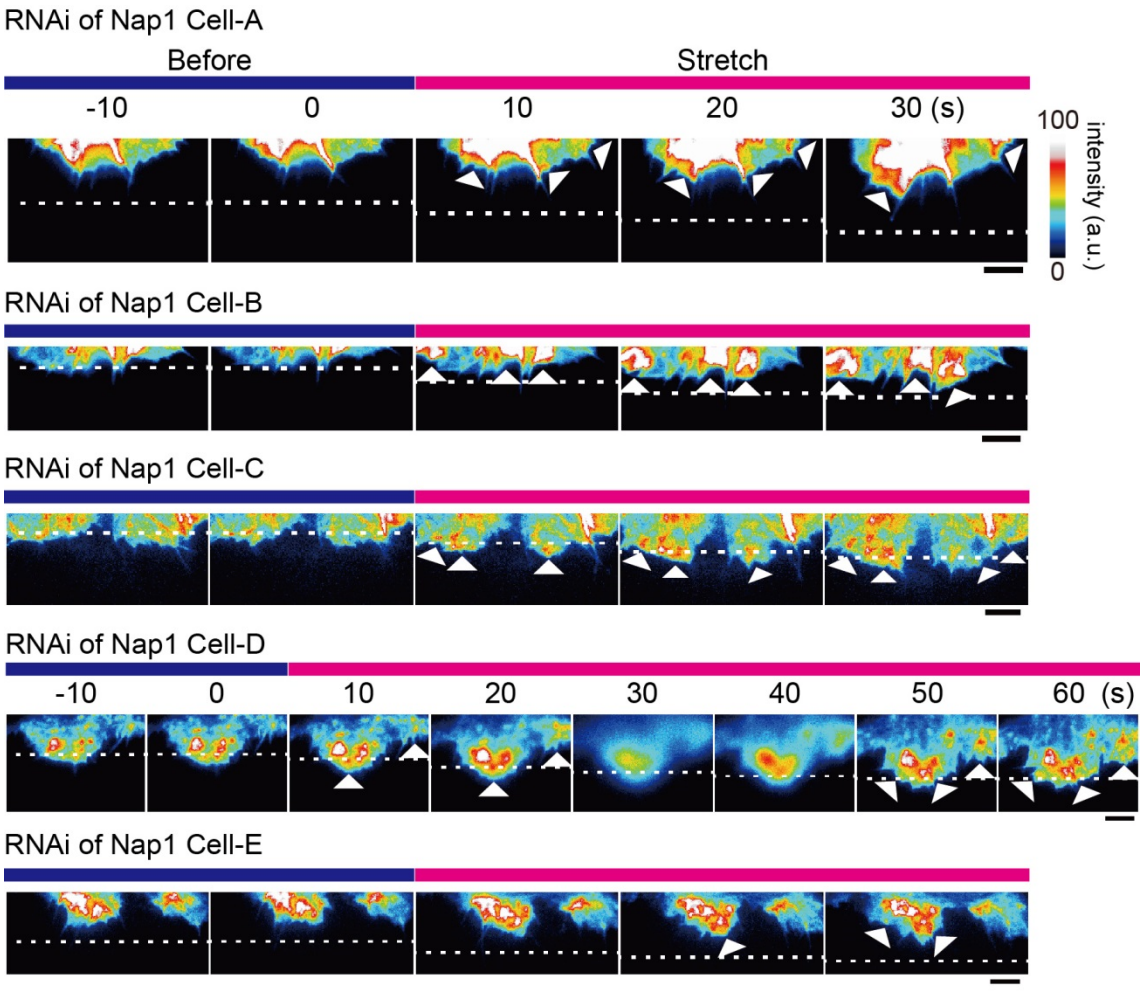

The stretch-induced actin network formation is observed in cells with impaired formation of the WAVE complex (all other cases of Fig. S8b experiments).

Time lapse images of EGFP-actin in five cells are shown. White lines indicate the vertical position of the center of a bead buried into the PDMS substrate. Time is the same as shown on the top of Cell-A images. Arrowheads indicate lamellipodium tip areas associated with enhanced EGFP-actin signals. In cells A-D, the increase in the density of the new actin network was observed. Scale bars, 5 μm.

Figure S10

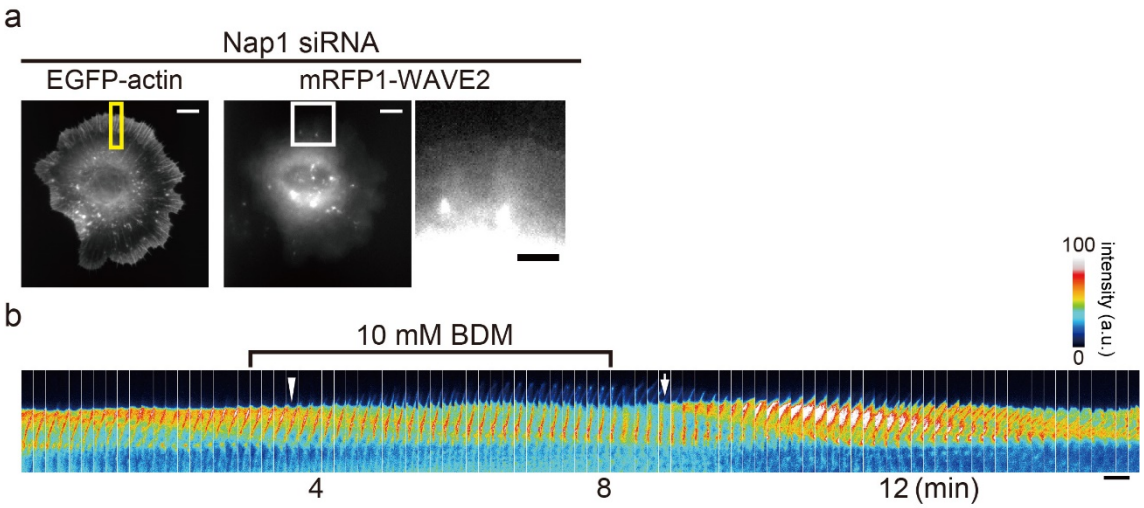

Depletion of the WAVE complex does not affect the BDM-induced reduction in actin assembly at the lamellipodium tip

(**a**, **b**) In **a**, images of Nap1 knock down cell are shown. EGFP-actin was co-expressed with mRFP1-WAVE2. Images in a yellow rectangle are shown in **b**. Boxed region in the image of mRFP1-WAVE2 is shown in the right of original image. Scale bar, 10 μm. In **b**, an arrowhead indicates the reduction of EGFP-actin fluorescence from the cell leading edge by BDM treatment. An arrow indicates the recovery of the density of the actin network after was out. Scale bar, 5 μm.

Figure S11

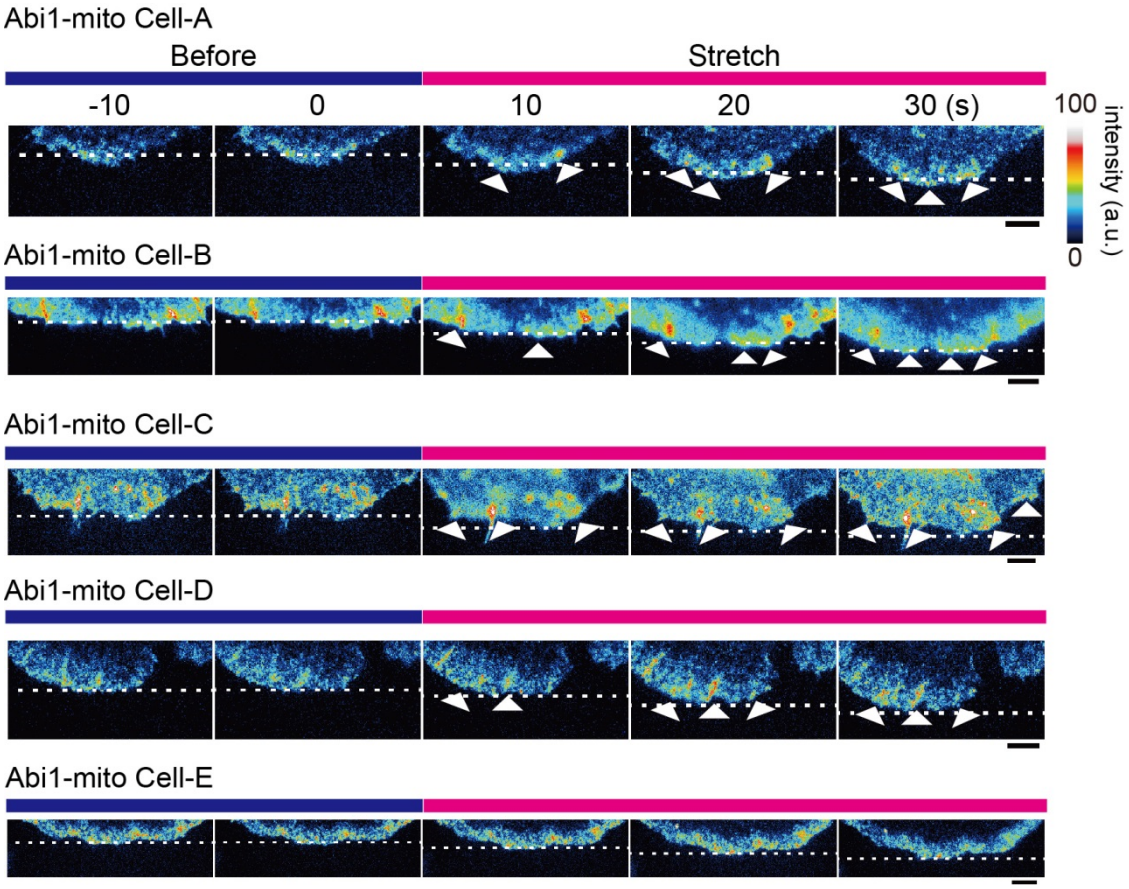

Stretch-induced actin assembly in cells where the WAVE complex is depleted from the cell edge by Abi1-mito overexpression (all other cases of Fig. S5d experiments)

Time lapse images of GFP from five cells co-expressing a high level of mRFP1-Abi1-mito and EGFP-actin. White lines indicate the vertical position of the center of a bead buried into the PDMS substrate. Time is the same as shown on the top of Cell-A images. Arrowheads indicate lamellipodium tip areas associated with enhanced EGFP-actin signals. In cell A and B, the increase in the density of the new actin network was observed. The marginal increase in the density of the new actin network was induced in cell C and D. Scale bars, 5 μm.

Figure S12

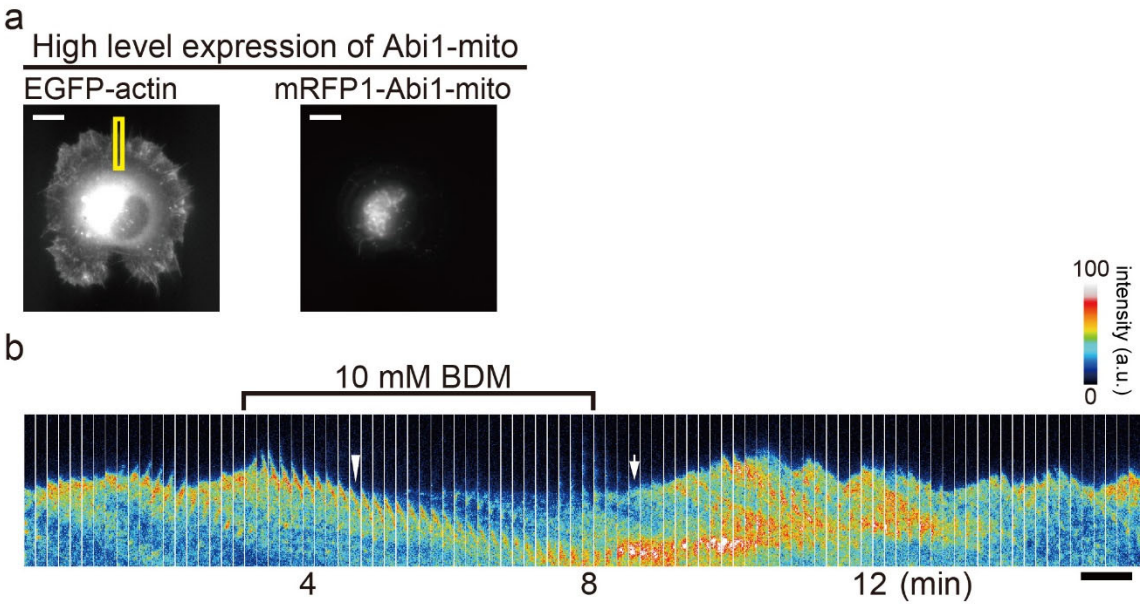

Reduction in actin assembly at the lamellipodium tip upon BDM treatment in cells expressing a high level of Abi1-mito

(**a**, **b**) In **a**, images of a cell co-expressing mRFP1-Abi1-mito at a high level and EGFP-actin are shown. Scale bar, 10 μm. Images in a yellow rectangle are shown in **b**. Scale bar, 10 μm. In **b**, an arrowhead indicates the reduction in the EGFP-actin fluorescence from the cell leading edge by BDM treatment. An arrow indicates the recovery of the density of the actin network after wash out. Scale bar, 5 μm.

Figure S13

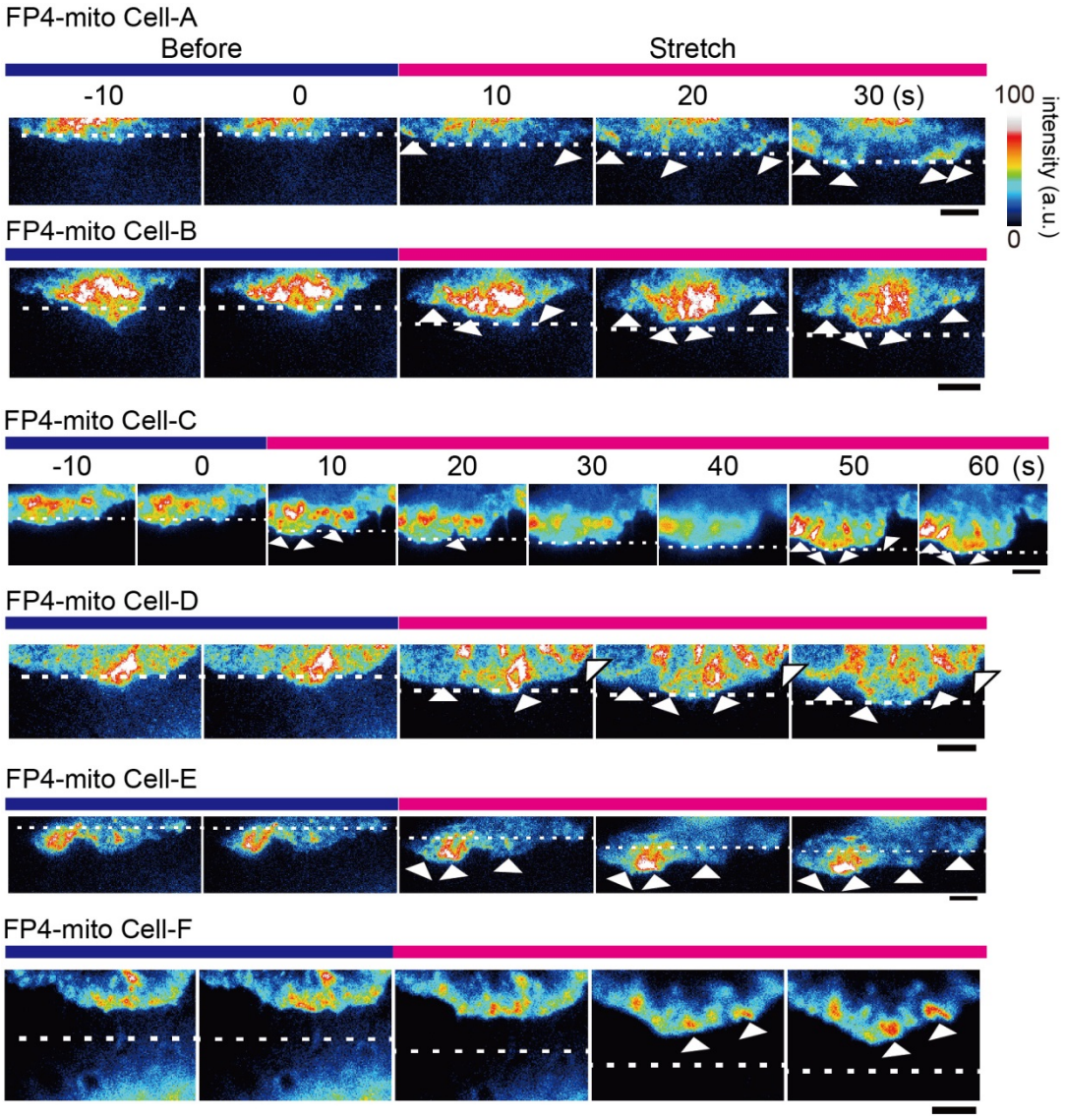

Stretch-induced dense actin network formation at the edge of cells expressing a high level of FP4-mito (all other cases of Fig. S8f experiments)

Time lapse images of GFP from the six cells co-expressing mRFP1-FP4-mito at high level and EGFP-actin are shown. White lines indicate the vertical position of the center of a bead buried into the PDMS substrate. Time is the same as shown on the top of Cell-A images. Arrowheads indicate lamellipodium tip areas associated with enhanced EGFP-actin signals. In cell A-C, the increase in the density of the new actin network was observed. The marginal increase in the density of the new actin network was induced in cell D and E. Scale bars, 5 μm.

Figure S14

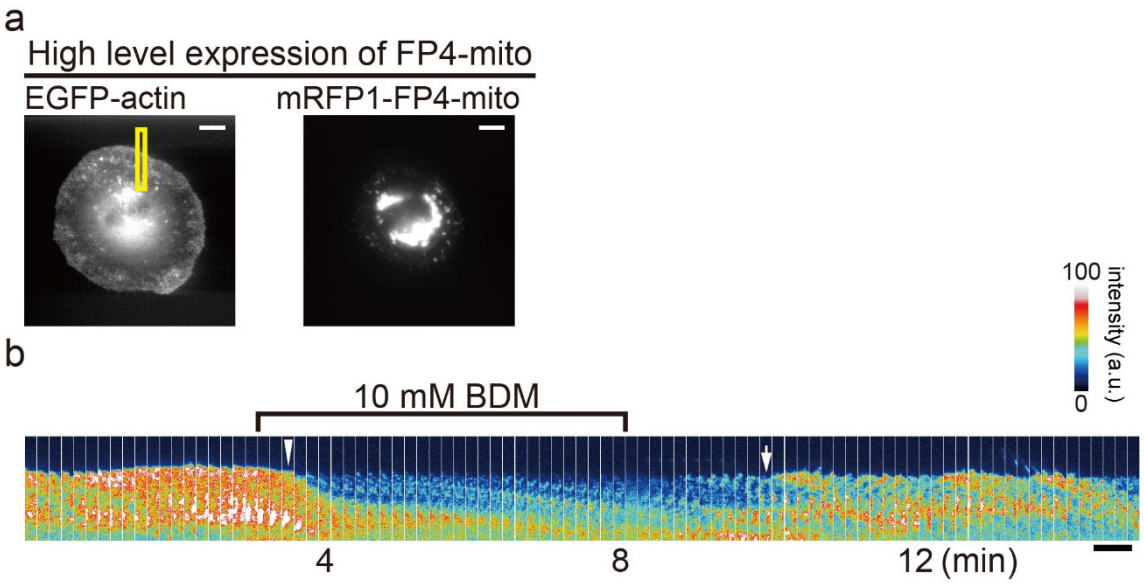

BDM attenuates actin assembly at the lamellipodium tip in the absence of Ena/VASP proteins

(**a**, **b**) In **a**, images of the cell co-expressing mRFP1-FP4-mito at high level and EGFP-actin are shown. Scale bar, 10 μm. Images in a yellow rectangle are shown in **b**. Scale bar, 10 μm. In **b**, an arrowhead indicates the reduction in the density of the actin network from the cell leading edge upon BDM treatment. An arrow indicates the recovery in the EGFP-actin signals after wash out. Scale bar, 5 μm.

Figure S15

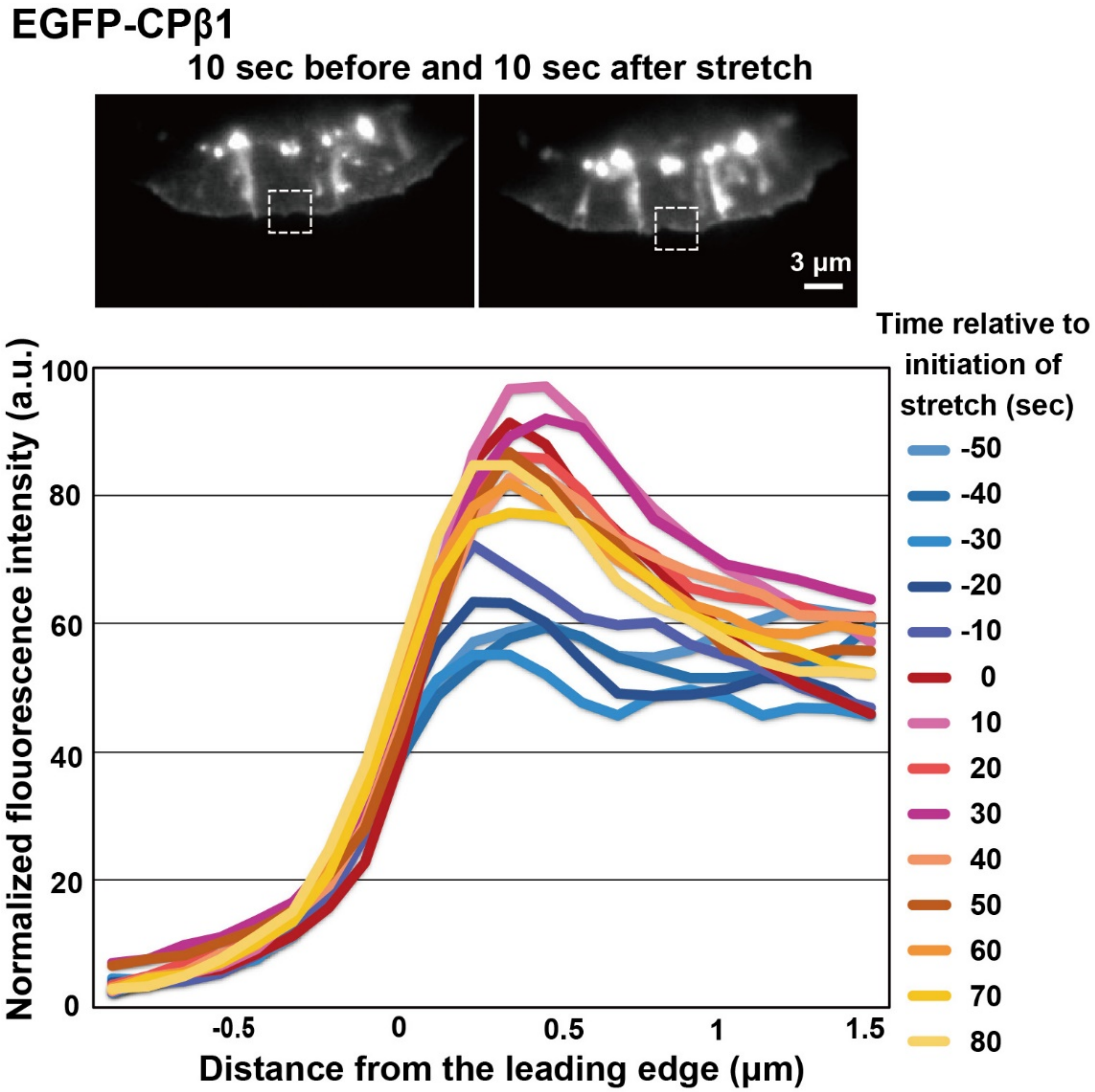

Leading edge association of Capping Protein increases in response to cell edge stretch.

The graph shows the intensity of EGFP-CPβ1 along the line perpendicular to the cell contour measured using the Line Scan command of the Metamorph software (average of 5 experiments; intensity was normalized for peak fluorescence of each measurement). Representative images of EGFP-CPβ1 before and after initiation of the stretch are shown on the top. The regions indicated by boxes were used for the measurement. The data indicate that barbed end uncapping is not a mechanism for the stretch-induced lamellipodium tip actin assembly.

Figure S16

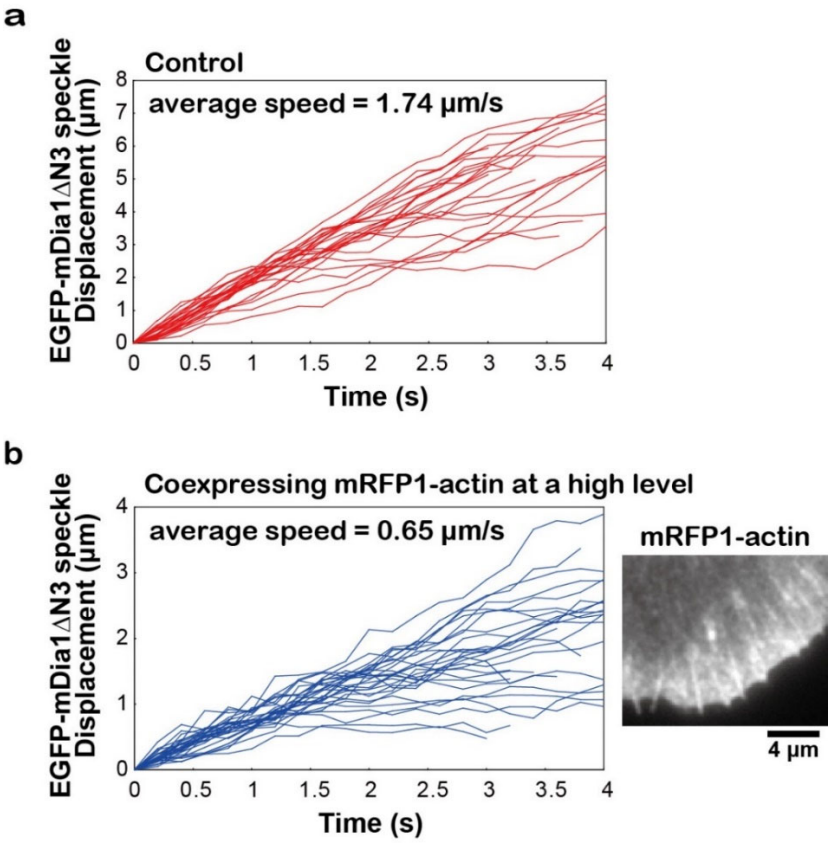

Impaired processive actin polymerization by formin homology proteins in cells overexpressing mRFP1-actin

Our previous study (*Mol. Biol. Cell* 25, 1010-1024, 2014) reported impaired processive actin elongation by mDia1ΔN3 (composed of FH1 and FH2 domains, aa 543-1192) in cells overexpressing mRFP1-actin. The average speed of mDia1ΔN3 SiMS including the stopping phase is calculated and shown on the graph for a control cell (**a**) (n = 24) and a cell overexpressing mRFP1-actin (**b**) (n = 28). The average speed in **a** is comparable to the data in our previous study (*Science* 303, 2007-2010, 2004) and it was reduced to 37% of control in **b**. Because the cell in **b** expresses a comparable amount of fluorescent protein-tagged actin (the right image) to those used in Figure 1 and Figure S3 analyses, the stretch-induced increase in EGFP-actin signals at the lamellipodium tip is not attributable to the activity of formin homology proteins. It is important to note that EGFP-actin not only impairs the formin-mediated processive actin elongation but also poorly incorporates into formin-assembled F-actin. The graphs and the image are reproduced from *Mol. Biol. Cell* 25, 1010-1024, 2014.

Captions for Supplementary Movies

Movie 1

Stretch manipulation increases the density of EGFP-actin at the cell edge.

The left and right movies show images of EGFP-actin (left) and bright field (right) during stretch manipulation (Figure 1). Time is in minute:second. Scale bar, 10 μm.

Movie 2

Stretch manipulation increases the density of EGFP-actin at the cell edge (other examples of Figure 1).

Time-lapse movie shows images of EGFP-actin during stretch manipulation (Figure S3). White lines indicate the vertical position of the center of a bead buried into the PDMS substrate. Time is in minute:second. Scale bars, 5 μm.

Movie 3

Stretch manipulation increases the number of new actin SiMS near the cell edge.

The left and right movies show images of DL-actin (left) and bright field (right) during stretch manipulation (Figure 2a and b). Time is in minute:second. Scale bar, 10μm.

Movie 4

Cells retract after cytochalasin D treatment.

Time-lapse movie shows images of PKH26-stained XTC (green) on non-stretched substrate (gray) during cytochalasin D treatment (top of Figure 5a). Cells were treated with 5 μM cytochalasin D at 0:00. Time is in minute:second. Scale bar, 10 μm.

Movie 5

Cytochalasin D-induced cell edge retraction is attenuated in cells on the stretched substrate.

Time-lapse movie shows images of PKH26-stained XTC (green) on stretched substrate (gray) during cytochalasin D treatment (bottom of Figure 5a). Cells were treated with 5 μM cytochalasin D at 0:00. Time is in minute:second. Scale bar, 10 μm.

Movie 6

BDM treatment reduces the density of the actin network at the cell edge.

Time-lapse movie shows images of EGFP-actin during BDM treatment (Figure S6a and b). Cells were treated with 10 mM BDM from 3:00 to 8:00. Time is in minute:second. Scale bar, 10 μm.

Movie 7

BDM treatment reduces the number of new actin SiMS near the cell edge.

Time-lapse movie shows images of DL-actin during BDM treatment (Figure S6c). Twenty mM BDM was treated from 1:30 to 3:30. Time is in minute:second. Scale bar, 10 μm.

Movie 8

The increase in the density of EGFP-actin upon stretch is observed in Nap1 knockdown cells.

Time-lapse movie shows images of EGFP-actin during stretch manipulation in Nap1 knockdown cell (Figure S8b). White lines indicate the vertical position of the center of a bead buried into the PDMS substrate. Time is in minute:second. Scale bar, 5 μm.

Movie 9

The increase in the density of EGFP-actin upon stretch is observed in Nap1 knockdown cells (all other cases of Fig. S8b experiments).

Time-lapse movies show images of EGFP-actin during stretch manipulation in Nap1 knockdown cells (Figure S9). White lines indicate the vertical position of the center of a bead buried into the PDMS substrate. Time is in minute:second. Scale bars, 5 μm.

Movie 10

The reduction in the density of EGFP-actin upon BDM treatment is observed in Nap1 knockdown cells.

Time-lapse movie shows images of EGFP-actin during BDM treatment in Nap1

knockdown cells (Figure S10). Cells were treated with 10 mM BDM from 3:00 to 8:00. Time is in minute:second. Scale bar, 10 μm.

Movie 11

The increase in the density of EGFP-actin upon stretch is observed in cells expressing a high level of Abi1-mito.

Time-lapse movie shows images of EGFP-actin during stretch manipulation in the cell expressing high level of Abi1-mito (Figure S8d). White lines indicate the vertical position of the center of a bead buried into the PDMS substrate. Time is in minute:second. Scale bar, 5 μm.

Movie 12

The increase in the density of EGFP-actin upon stretch is observed in cells expressing a high level of Abi1-mito (all other cases of Fig. S8d experiments).

Time-lapse movies show images of EGFP-actin during stretch manipulation in the cell expressing high level of Abi1-mito (Figure S11). White lines indicate the vertical position of the center of a bead buried into the PDMS substrate. Time is in minute:second. Scale bars, 5 μm.

Movie 13

The reduction in the density of EGFP-actin upon BDM treatment is observed in cells expressing a high level of Abi1-mito.

Time-lapse movie shows images of EGFP-actin during BDM treatment in the cell expressing high level of Abi1-mito (Figure S12). Ten mM BDM was prefused from 3:00 to 8:00. Time is in minute:second. Scale bar, 10 μm.

Movie 14

The increase in the density of EGFP-actin upon stretch is observed in cells expressing a high level of FP4-mito.

Time-lapse movie shows images of EGFP-actin during stretch manipulation in the cell expressing high level of FP4-mito (Figure S8f). White lines indicate the vertical position

of the center of a bead buried into the PDMS substrate. Time is in minute:second. Scale bar, 5 μm.

Movie 15

The increase in the density of EGFP-actin upon stretch is observed in cells expressing a high level of FP4-mito (all other cases of Fig. S8f experiments).

Time-lapse movies show images of EGFP-actin during stretch manipulation in the cell expressing high level of FP4-mito (Figure S13). White lines indicate the vertical position of the center of a bead buried into the PDMS substrate. Time is in minute:second. Scale bars, 5 μm.

Movie 16

The reduction in the density of EGFP-actin upon BDM treatment is observed in cells expressing high level of FP4-mito.

Time-lapse movie shows images of EGFP-actin during BDM treatment in the cell expressing high level of FP4-mito (Figure S14). Ten mM BDM was perfused from 3:00 to 8:00. Time is in minute:second. Scale bar, 10 μm.